

University of Texas at Arlington

MavMatrix

Civil Engineering Theses

Civil Engineering Department

2022

Experimental Study of Flow Characteristics and Geometry of Scour Hole Around Cylindrical Piers Subject to Wave and Current

Qazi Ashique E Mowla

Follow this and additional works at: https://mavmatrix.uta.edu/civilengineering_theses



Part of the [Civil Engineering Commons](#)

Recommended Citation

Mowla, Qazi Ashique E, "Experimental Study of Flow Characteristics and Geometry of Scour Hole Around Cylindrical Piers Subject to Wave and Current" (2022). *Civil Engineering Theses*. 429.
https://mavmatrix.uta.edu/civilengineering_theses/429

This Thesis is brought to you for free and open access by the Civil Engineering Department at MavMatrix. It has been accepted for inclusion in Civil Engineering Theses by an authorized administrator of MavMatrix. For more information, please contact leah.mccurdy@uta.edu, erica.rousseau@uta.edu, vanessa.garrett@uta.edu.

EXPERIMENTAL STUDY OF FLOW CHARACTERISTICS AND
GEOMETRY OF SCOUR HOLE AROUND CYLINDRICAL PIERS SUBJECT
TO WAVE AND CURRENT

By

Qazi Ashique E Mowla

Thesis

Presented to the Faculty of the Graduate School of
The University of Texas at Arlington in Partial Fulfillment
of the Requirements for the Degree of

MASTER OF SCIENCE IN CIVIL ENGINEERING

The University of Texas at Arlington

August 2022

Supervising Committee:

Habib Ahmari, Supervising Professor

Nick Fang

Jessica Eisma

Copyright © by Qazi Ashique E Mowla, 2022

All Rights Reserved



ABSTRACT

This thesis concerns the unique flow structure around bridge piers under the wave and current conditions. The flow characteristics around piers may change depending on the flow conditions and geometry of the pier. These flow structures imprint themselves on the streambed as scour holes. Laboratory experiments were conducted to investigate the changes that occur in the flow pattern and in the geometric pattern of scour holes around piers in waterbodies subject to waves and currents. Physical models of two piers with different diameters (19 mm and 50 mm) were built and installed in a sediment bed. A total of 19 sets of experiments were conducted on three types of flow conditions: waves alone; current alone; and waves and current combined, in which the direction of the wave propagation was opposite the direction of the current. The effects of variables such as flow velocity, water depth, wave height, wave period, and pier size were studied to determine their influence on the geometry of scour holes. The data obtained from the laboratory experiments showed that scour holes were largest in flow with a steady current and smallest in water with only waves. The combination of waves and current produced scour depths larger than those of the waves-alone experiments but smaller than those conducted in water with only currents. Particle image velocimetry (PIV) was utilized to visualize the flow structure around piers under various flow conditions. A horizontal plane view of the flow field was analyzed and changes in vortex characteristics were investigated. Higher flow velocity produced stronger vortices in a steady current. For the waves-alone cases, when the pier was smaller in diameter, more scour was observed. The flow structure in the combined waves and current experiments was much more complex, although the flow characteristics were dominated by the current, the flow pattern around the pier was affected by the wave characteristics as well. Velocity vectors obtained from the PIV analysis showed that the mean displacement of sediment particles was in the same direction as the

current. The presence of negative velocity was also observed when the wave motion was against the current.

Finally, an attempt was made to relate the size of the vortices to the scour process. A clear-water flow regime was designed to ensure that the sediment movement that occurred during the experiments was caused by the pier in the sediment bed disturbing the flow structure. The results showed that the strength of wake vortices, the relative direction of the flow, and the distances of waves from the channel bottom influenced the scour pattern around the cylindrical pier and the downstream deposition pattern.

ACKNOWLEDGEMENT

I would like to express my eternal gratitude to my supervisor, Dr. Habib Ahmari, for providing me the opportunity to work under his supervision and making me a part of his research team. His continuous guidance, support, and patience were the primary sources of my motivation behind this thesis. His professionalism, along with his unique and innovative ways of dealing with problems, has always amazed me and will always have an influence on my academic and professional career.

I would also like to express my sincere gratitude to the members of my thesis committee, Drs. Nick Fang, and Jessica Eisma, for their valuable comments, and to Mr. Qays Mohammed, technical staff member at the hydraulics and fluid mechanics lab, UTA. His knowledge and his technical expertise helped me a lot when I was building the physical model. I wish to acknowledge my friend and ex-colleague Shah Md Imran Kabir who helped me and shared his valuable insights regarding my work whenever I needed them. Over time, he became like a brother to me whom I look up to.

I am grateful to Niloy Gupta, Alinda Gupta, Tasfinul Haque, and Humaun Kobir and all those who helped and supported me throughout this journey. I also thank my sister Qazi Aniqua Zahra and my brother-in-law Zabir Ahmed for their motivation and prayers.

My wife Afia Anjum Ananya and my parents Dr. Qazi Azizul Mowla and Dr. Syeda Sayeeda deserve special recognition. My parents, who taught me to dream big, are my constant source of inspiration. My wife, who took care of every household chore, did not let me worry about anything except my thesis for the last few months, and kept pushing me to be the best I can be, deserves my sincere gratitude.

Last but greatest thanks to my Almighty for all the blessings HE has bestowed on me during this period.

TABLE OF CONTENTS

ABSTRACT.....	i
ACKNOWLEDGEMENT	iii
TABLE OF CONTENTS.....	iv
LIST OF FIGURES	vii
LIST OF TABLES.....	x
CHAPTER 1 INTRODUCTION.....	1
1.1. Background and Motivation.....	1
1.2. Research Objective and Plan.....	3
1.3. Thesis Organization.....	4
CHAPTER 2 LITERATURE REVIEW.....	5
2.1. Scour Process	5
2.2. Types of Scour	6
2.2.1. General Scour.....	6
2.2.2. Localized Scour	7
2.3. Factors Affecting Scour Depth.....	9
2.4. Scour Hole Shape and Size	10
2.5. Mechanism and Prediction of Scour	13
2.5.1. Scour Around Piers in Current-alone Cases	14
2.5.2. Scour Around Piers in Wave-alone Cases	17
2.5.3. Scour Around Piers Under Combined Waves and Current	20
2.6. Timescale	23
2.7. Employing Particle Image Velocimetry (PIV) to Visualize Flow Around Piers	25
2.7.1. Typical Flow Structure Around a Cylindrical Pier.....	25
2.7.2. PIV Components.....	26
2.7.3. Application of PIV for Visualizing Flow Field Around Piers and Scour Holes.....	28
CHAPTER 3 METHODOLOGY.....	30
3.1. Introduction	30

3.2.	Experimental Flume	30
3.3.	Pier Models	31
3.4.	Flow Scenarios	32
3.4.1.	Waves-alone Experiments	32
3.4.2.	Current-alone Experiments	33
3.4.3.	Wave and Current Combined Experiments	34
3.5.	Measurement of Flow Parameters.....	35
3.5.1.	Flow Rate Measurement	35
3.5.2.	Velocity Measurement	35
3.5.3.	Flow Depth Measurement.....	36
3.6.	Preparation of the Sediment Bed.....	37
3.6.1.	Determination of Sediment Size	38
3.6.2.	Sieve Analysis.....	39
3.6.3.	Sediment Bed.....	40
3.7.	PIV Setup and Data Acquisition	42
3.7.1.	Laser.....	43
3.7.2.	Seeding Particles.....	43
3.7.3.	Camera	43
3.7.4.	Post Processing (PIVLab).....	43
3.8.	Flow Conditions	44
CHAPTER 4 RESULT AND DISCUSSION.....		46
4.1.	Introduction	46
4.2.	Scour Hole Geometry Subject to Different Flow Conditions	46
4.2.1.	Waves-alone Cases	46
4.2.2.	Current-alone Cases	50
4.2.3.	Combined Wave and Current Cases	54
4.3.	Flow Structure Around Piers Subject to Different Flow Conditions	58
4.3.1.	Waves-alone Cases	59
4.3.2.	Current-alone Cases	61
4.3.3.	Combined Wave and Current Cases	65
4.4.	Relation Between the Flow Structure Around Piers and the Scour Hole Geometry.....	68

4.4.1. Waves-alone Cases	68
4.4.2. Current-alone Cases	70
4.4.3. Combined Waves and Current Cases.....	71
CHAPTER 5 CONCLUSIONS AND FUTURE RESEARCH RECOMMENDATIONS ..	73
5.1. Summary and Conclusions.....	73
5.2. Recommendations for Future Research	75
References.....	77
APPENDIX A SAMPLE CALCULATIONS	82
APPENDIX B GRADATION ANALYSIS	87

LIST OF FIGURES

Figure 1.1. Causes of bridge failures in the U.S. from 1980 – 2012 (Lee et al., 2013)	2
Figure 2.1. Hierarchy showing the classification of total scour (Gazi et al., 2019).....	6
Figure 2.2. Different types of scour in a typical bridge cross-section (Wang, 2004)	7
Figure 2.3. Typical wave-induced scour hole (Kobayashi and Oda 1994).....	11
Figure 2.4. Relationship between the scour type and KC number in different sand samples collected from five places in Japan (Kobayashi and Oda 1994).....	12
Figure 2.5. Scour pattern around a cylindrical bridge pier in current-only condition (Akhlaghi et al., 2020)	15
Figure 2.6. Flow field around a pier under wave-alone conditions ($6 < KC < 100$) (Gazi et al., 2019)	18
Figure 2.7. Wave-induced local pier scour depth ratio (S_{max}/D) as a function of Keulegan-Carpenter number (KC) (Webb and Matthews 2014).....	20
Figure 2.8. Flow field around a pier under combined wave-current conditions (Qi and Gao 2014)	22
Figure 2.9. Evolution of equilibrium scour depth, $S_r(t)$ at time t	24
Figure 2.10. Type of flow regime around a circular cylinder in oscillatory flow at different KC numbers (Sumer and Fredsøe 2006)	26
Figure 2.11. Typical arrangement for particle image velocimetry (PIV) (Sim and Fane 2017)..	27
Figure 3.1. Schematic diagram of the experimental flume (not to scale)	31
Figure 3.2. The 19 mm and 50 mm piers used in this study	32
Figure 3.3. (a) Side view of the wave generator connected to the speed controller, with lever arm installed near the flume outlet; (b) wave absorber and flow straightener near the flume inlet.....	33
Figure 3.4. (a) Modification to the wave generator flap to run wave-current experiments, (b) modified wave generator in action.....	34
Figure 3.5. Acoustic doppler velocimeter (ADV) used to measure the velocity	36
Figure 3.6. Schematic of the laboratory flume and sediment bed.....	37
Figure 3.7. (a) #14, #16, #18, #20, and #25 sieves were used to obtain uniform sand for the sediment bed, (b) sieve test apparatus.....	39
Figure 3.8. Sediment bed for the scour experiments.....	41

Figure 3.9. Local scour observed near the edge of the sediment bed	41
Figure 3.10. Experimental arrangement for the particle image velocimetry	42
Figure 4.1. Scour under wave-only cases: (a) $KC < 6$ (50 mm pier), and (b) $KC > 6$ (19 mm pier)	49
Figure 4.2. Distribution of maximum scoured points under waves-alone flow condition.....	50
Figure 4.3. Scour around 50 mm pier in current-only experiments: (a) water depth = 10.2 cm, flow velocity = 15.3 cm/s; and (b) flow depth = 12.7 cm, flow velocity = 17.4 cm/s.....	53
Figure 4.4. Scour around piers in current-only experiments: (a) 50 mm pier, water depth = 15.2 cm, flow velocity = 27.2 cm/s; (b) 19-mm pier, water depth = 10.2 cm, flow velocity = 15.9 cm/s	53
Figure 4.5. Scour around 19 mm pier in current-only experiments: (a) water depth = 12.7 cm, flow velocity = 17.4 cm/s; and (b) water depth = 15.2 cm, flow velocity = 27.2 cm/s	54
Figure 4.6. Scour around piers in waves and current combined experiments: (a) 50 mm pier, water depth = 15.2 cm, flow velocity = 15.3 cm/s; (b) 50 mm pier, water depth = 17.8 cm, flow velocity = 16.1 cm/s.....	57
Figure 4.7. Scour around piers in waves and current combined experiments : (a) 50 mm pier, water depth = 20.3 cm, flow velocity = 15.8 cm/s; (b) 50 mm pier, water depth = 25.6 cm, flow velocity = 16.1 cm/s.....	57
Figure 4.8. Scour around piers in waves and current combined experiments: (a) 19 mm pier, water depth = 15.2 cm, flow velocity = 15.3 cm/s; (b) 19 mm pier, water depth = 17.8 cm, flow velocity = 16.1 cm/s; (c) 19 mm pier, water depth = 20.3 cm, flow velocity = 15.9 cm/s.....	58
Figure 4.9. (a) Wave crest area crossing the pier, (b) wave trough area crossing the pier	59
Figure 4.10. Observed flow regimes for KC between 1.96 and 2.31: (a) wave crest area crossing the pier, (b) wave trough area crossing the pier.....	59
Figure 4.11. Observed flow regimes around pier under wave-only condition with KC range of 5.56-6.39: (a) wave crest area crossing the pier, (b) wave trough area crossing the pier	60
Figure 4.12. Observed flow regimes around the 19 mm pier for current alone cases: (a) flow depth = 10.2 cm, flow velocity = 15.7 cm/s; (b) flow depth = 12.70 cm, flow velocity = 17.4 cm/s velocity; and (c) flow depth 15.2 cm, flow velocity =27.2 cm/s	62
Figure 4.13. Time-averaged velocity distribution around a 19 mm circular cylinder	63

Figure 4.14. Flow regimes around the 50 mm pier for current alone cases : (a) 10.2-cm water depth, 15.9 cm/s velocity; (b) 12.7-cm water depth, 17.4 cm/s velocity; and (c) 15.2-cm water depth, 27.2 cm/s velocity	64
Figure 4.15. Time-averaged velocity distribution around a 50 mm circular cylinder	65
Figure 4.16. (a) Wave-crest area under waves against current, (b) wave trough area under waves against the current (Qi and Gao 2014).....	66
Figure 4.17. Flow pattern for KC range 4.53-5.04 coupled with a current from the opposite direction: (a) wave crest area crossing the pier, (b) wave trough area crossing the pier	66
Figure 4.18. Mean velocity field pattern around the 50 mm pier for combined wave and current cases: (a) wave-induced local flow in the same direction as the current direction, and (b) wave-induced local flow in the opposite direction as the current	68
Figure A.1. Grain size classification chart (Wensworth, 1922).....	84
Figure A.2. Shields diagram (adopted from Miedema, 2010)	85
Figure B.1. Sieve analysis of sediment bed soil (Sample 1).....	87
Figure B.2. Sieve Analysis of sediment bed soil (Sample 2).....	88
Figure B.3. Sieve Analysis of sediment bed soil (Sample 3).....	89

LIST OF TABLES

Table 3.1. Test Conditions for Flume Experiments (Waves propagating opposite to the current direction).....	44
Table 4.1. Test Conditions and Results for Local Scour Around a Cylindrical Pier: Waves-alone Cases	47
Table 4.2. Comparison of Calculated and Observed Equilibrium Scour Depth for Waves-alone Cases	48
Table 4.3. Test Conditions and Test Results for Local Scour Around a Cylindrical Pier: Current-alone Cases.....	51
Table 4.4. Comparison of Observed Scour Depth with Calculated Values from Other Studies .	52
Table 4.5. Test Conditions and Results for Local Scour Around a Cylindrical Pier: Wave and Current Combined Cases	55
Table 4.6. Comparison of Observed Scour Depth with Calculated Values from Other Studies .	56
Table 4.7. Vortex Characteristics Under Different Flow Scenarios of Current-alone Cases.....	65
Table A.1. Determination of Appropriate Sediment Size to Maintain a Clear-Water Regime....	86
Table B.1. Gradation Analysis of Sediment Bed Soil (Sample 1)	87
Table B.2. Gradation Analysis of Sediment Bed Soil (Sample 2)	88
Table B.3. Gradation Analysis of Sediment Bed Soil (Sample 3)	89

CHAPTER 1

INTRODUCTION

1.1. Background and Motivation

Bridge failures have far-reaching and devastating effects. They cause fatalities, hamper emergency response and evacuation after disasters, and result in immense economic loss. Scour is one of the major causes of bridge failure as, along with floods, it contributes to more than 60% of the bridge failures in the U.S. (Hunt, 2009; Ahamed et al., 2020). Approximately 83% of the 580,000 bridges in the United States cross waterways, which means they may require scour consideration (National Research Council, 2005). More than 20,000 of them are classified as scour critical, which means that one of every 34 is vulnerable to scour. Lee et al. (2013) collected data on the causes of bridge failures from 1980 to 2012 and found that scouring was the reason for 20% of the bridge failures in the U.S. Flood, overload, collision, internal forces, and environmental degradation are also predominant factors, and although flood and scour are reported separately in **Figure 1.1**, they are closely related. Bridge failures due to floods occur either because of the high hydrodynamic forces exerted on the superstructures (decks and girders) or because of the intense flow that may cause scour around the substructures (piers and abutments). Scour can occur any time, but it accelerates during a flood event.

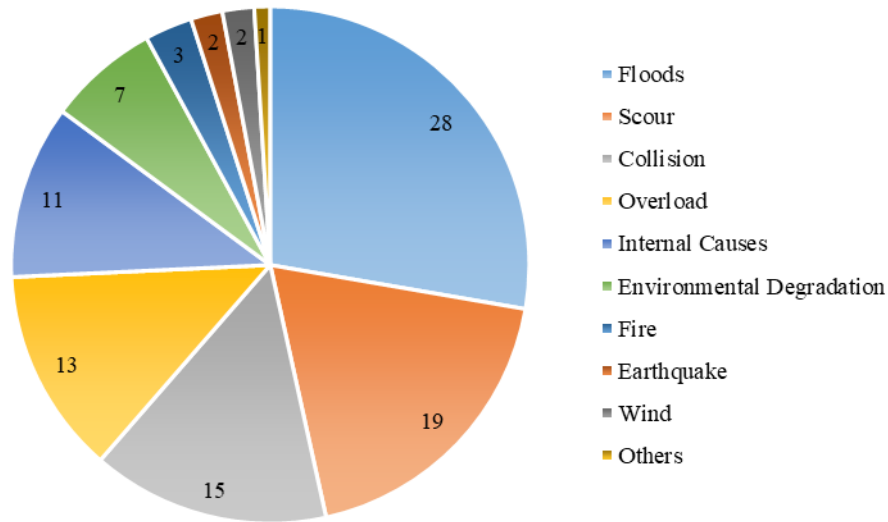


Figure 1.1. Causes of bridge failures in the U.S. from 1980 – 2012 (Lee et al., 2013)

Numerous studies have been conducted on the prediction of scour around bridge piers, and various equations have been developed to calculate the equilibrium scour depth. Most of them have investigated piers in riverine conditions, representing stream-crossing bridges, but a limited number studied wave-alone conditions, representing the coastal environment, and an even smaller number considered the combined conditions of waves and currents, representing the lacustrine environment. Most of them investigated or modeled the scour pattern rather than exploring its cause. The Federal Highway Administration’s (FHWA’s) manuals, FHWA HEC-18 (Evaluating Scour at Bridges), and FHWA HEC-25 (Highways in the Coastal Environment) provide scour prediction equations and guidelines for riverine, coastal, and lacustrine environments. The scour mechanism in coastal and lacustrine environments is very complex. The relative direction of the waves and current can change the flow structure and eventually affect the scouring process. Many of these scenarios have not yet been investigated. When the flow meets the pier, flow features such as the downward flow, horseshoe vortices, and wake vortices are created. Horseshoe vortices dominate the scouring process, which is why most of the studies investigating the flow structure

around piers focus on them. Wake vortices created downstream of the pier are also responsible for scouring and are responsible for the size and shape of the scour around piers. Where horseshoe vortices increase the flow velocity near the bed, wake vortices carry the eroded bed downstream (Melville and Coleman 2000).

Collecting data on the major flow structures (downflow, horseshoe vortex, wake vortices) around piers, and investigating their effects on flow conditions is challenging. The most commonly used tools for capturing turbulent flow characteristics are the Acoustic Doppler Velocimeter (ADV) and the Laser Doppler Velocimetry (LDV), but the point measurements that they take are time-consuming for large areas. The use of Particle Image Velocimetry (PIV), a comparatively new technology, can eliminate this issue, but to the author's best knowledge, very few studies have utilized it for this purpose thus far. It is usually applied in the controlled environment of a laboratory to investigate the structure of flow around a physical model.

1.2. Research Objective and Plan

The main objective of this study was to investigate the flow characteristics around cylindrical piers and the resulting scour hole geometry. This was accomplished by performing the following tasks:

1. Investigating the local scour geometry around cylindrical piers under different flow conditions
2. Utilizing Particle Image Velocimetry (PIV) to investigate the flow structure around piers
3. Comparing the sizes and shapes of scour holes with the flow patterns around the piers
4. Justifying the size and shape of the scour as the footprint of the vortex forms around piers

1.3. Thesis Organization

This thesis consists of five chapters. Chapter 1 provides information on the motivation, background, and objective of the research. Chapter 2 discusses the relevant literature on the scour process, mechanism, and geometry under different flow conditions and the application of PIV for analyzing local scour. Chapter 3 presents the procedures that were followed to design the experimental setup and perform the data collection to fulfill the research objectives. Chapter 4 reveals the test results obtained from the laboratory experiments and interprets, evaluates, and analyzes them. A summary of the research is presented in Chapter 5, along with recommendations for future work.

CHAPTER 2

LITERATURE REVIEW

2.1. Scour Process

According to the U.S. Federal Highway Administration (FHWA), scour is the removal of bed/bank material surrounding a bridge foundation. It is the result of the erosive force of water that excavates and carries away material from the bed and banks of waterbodies and from around bridge piers and abutments (Gazi et al., 2019). Scouring is one of the primary causes of bridge failures in the U.S., and its characteristics vary with the flow environment (Lee et al., 2013). For example, the mechanism of scour in riverine environments is different from those under wave action, i.e., coastal and lacustrine environments. In riverine environments, the unidirectional flow creates the scour hole. In coastal areas, lakes, and reservoirs, flow is multi-directional. Although the flow in both coastal areas and lake/reservoir areas is multi-directional, they are different from each other. In lakes and reservoirs, both waves and currents are present, whereas in a coastal environment – the wave action causes scouring.

Scour can occur at any time, but beds and banks are more susceptible to scouring during flood events. A number of forces contribute to scouring. It begins when the drag and lift forces are greater than the sediment particle mass and is exacerbated during a flood condition, when the forces, which are related to fluid motion, are larger than normal. Scour reaches its maximum near the flood's peak, but weakens as the water recedes (Gazi et al., 2019; Eadie and Herbich 1986). Scour also depends on the type of bed material. Loose sediment, like sands or fine gravel, erode rapidly, sometimes in a matter of hours; cohesive or cemented sediment erodes in days; sandstone, glacial till, shale, etc. take a few months to erode; limestone requires years, and granites erode over

centuries. The equilibrium scour depth is almost the same, however, for cohesive and non-cohesive sediments (Gazi et al., 2019). Non-cohesive sediment was used in this study.

2.2. Types of Scour

The different types of scour that may be in the vicinity of a bridge structure are shown in **Figure 2.1**. Since they are independent of each other and stem from different causes, the calculation for predicting the total scour requires that each type be calculated separately and then totaled (Sreedhara et al., 2015).

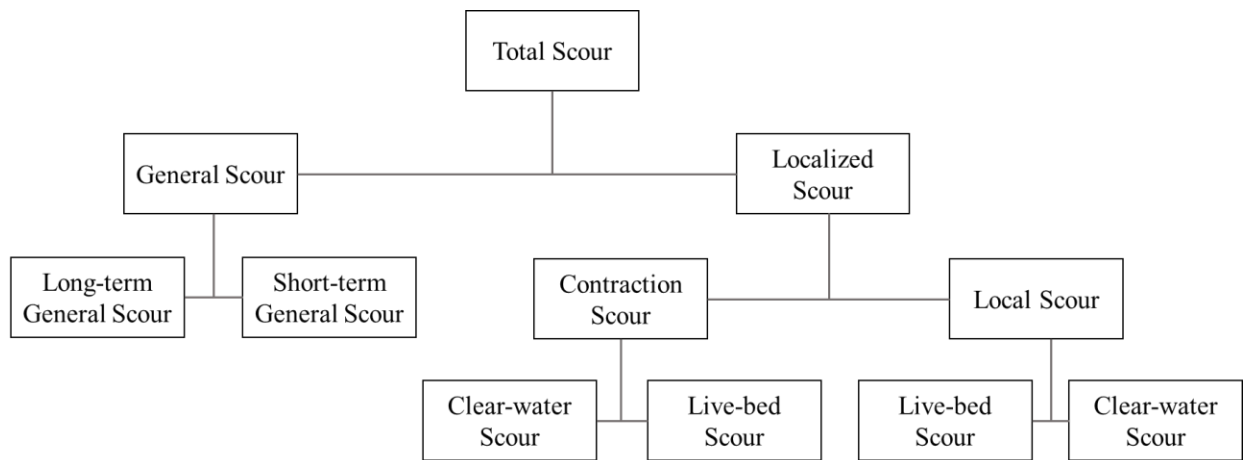


Figure 2.1. Hierarchy showing the classification of total scour (Gazi et al., 2019)

2.2.1. General Scour

General scour is the natural reduction of the riverbed elevation and does not depend on the location of the bridge or structure (Thomas, 2021). It can be categorized into long-term general scour and short-term general scour, as shown in **Figure 2.1**. The former takes place over a period of time that is long enough to reduce the elevation of the bed and occurs over the entire reach of the waterbody. General scour typically refers to short-term general scour – scour that occurs over a

relatively short period of time (Sreedhara et al., 2015). Since this type of scour has nothing to do with the existence of a structure, it was not considered in this study.

2.2.2. Localized Scour

Scour that occurs in the vicinity of a structure is known as localized scour and is the most common type of scour around bridge components (piers, abutments, spurs, embankments, etc.) or other hydraulic structures (Thomas, 2021). Localized scour is further divided into contraction scour and local scour, and when it is near a structure, it is normally a combination of both types (**Figure 2.2**)

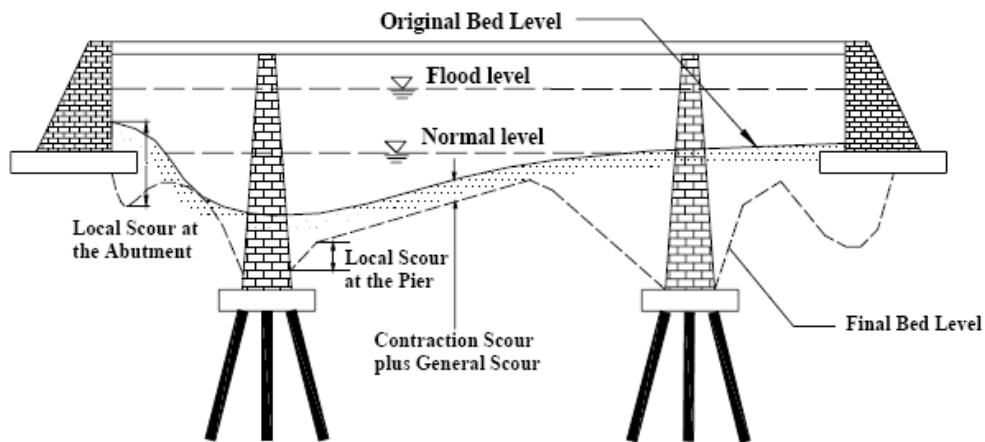


Figure 2.2. Different types of scour in a typical bridge cross-section (Wang, 2004)

Contraction Scour

Contraction scour occurs because of a reduction in the channel's cross-sectional area that is caused by either a natural contraction of a waterbody or a constructed feature (Ponce, 2011). From the conservation of mass formula, we know that when the flow area decreases, the flow velocity increases. Consequently, when there is a contraction in the channel cross-sectional area, both the local velocity and the bed shear stress increase. The resulting erosive force causes more bed material to leave than enter the area and results in the riverbed deepening (Sreedhara et al., 2015).

Local Scour

Local scour may occur when there is a change in the flow field due to the presence of a hydraulic structure or any other obstruction in the channel. Any type of structure in a channel obstructs the flow, causes interference, and results in various types of vortices being formed at the base and on the sides of the obstruction. Examples of places where this type of scouring occurs are around bridge piers, abutments, spur dikes, and river training works (Gazi et al., 2019).

Clear-Water Scour and Live-Bed Scour

Contraction and local scour can be further classified into two types, clear-water scour and live-bed scour, based on the sediment-carrying capacity of the flow. Clear-water scour occurs when there is no movement of the bed material upstream of a structure because the Froude number is low and the flow velocity is less than the critical velocity (Ponce, 2011). This is because the flow lacks the strength to initiate bed movement when the velocity is less than the critical velocity. On the contrary, when the Froude number is high and the flow velocity is higher than the critical velocity, the flow has enough strength to initiate bed movement. Live-bed scour occurs when sediment particles are transported by the approaching flow, and since there is a continuous supply of sediment, the scour hole continues to get filled. Live-bed scour is cyclical. During a flood event, scour that forms, when the water level rises, is replaced by sediment when the water level falls (Gazi et al., 2019).

In clear-water scour, the scour depth increases with the increasing velocity of flow until the velocity is close to the critical velocity. In this situation, scour depth no longer increases with time. This depth is known as the equilibrium scour depth, and it is the maximum clear water-scour depth (Kawata and Tsuchiya 1988). Typically, a clear-water regime is observed during low flow, when the sediment is coarse or the gradient is flat (Gazi et al., 2019). In live-bed scour, the equilibrium

scour depth is achieved when the rate of sediment flow to the scour hole is equal to the sediment outflow from the scour hole. This live-bed equilibrium scour depth is about 10% smaller than that of the clear-water equilibrium (Kawata and Tsuchiya 1988; Arneson et al., 2012). A clear-water regime was maintained in the laboratory flume for this study.

2.3. Factors Affecting Scour Depth

Many factors affect the depth of scour holes. Natural features like geomorphology of the catchment area, bed characteristics, or human activities such as building hydraulic structures or riverbed mining are some of the controlling factors for general scour. The contraction magnitude of the cross-sectional area affects contraction scour, as the width of a bridge's guide-bank or piers, or the presence of vegetation at the catchment area makes a waterway narrower and eventually results in channel deepening or scouring. Some of the controlling factors in local scour are the bridge geometry; type, shape, size, and orientation of the piers; flow depth, flow velocity, angle of attack, etc. (Khan et al., 2016).

The scour mechanism for non-cohesive and cohesive sediments is quite different. Cohesive sediments such as fine silt or clay have an electrochemical bonding that makes their erosion thresholds immune to influence from individual particles' properties. They are instead affected by physiochemical properties such as degree of saturation, drainage conditions, clay percentage, etc. The scouring mechanism of non-cohesive sediments is different. The bed's roughness changes with the size of the sediment and affects both the flow characteristics around the structure and the mobility of the bed material (Raikar and Dey, 2005).

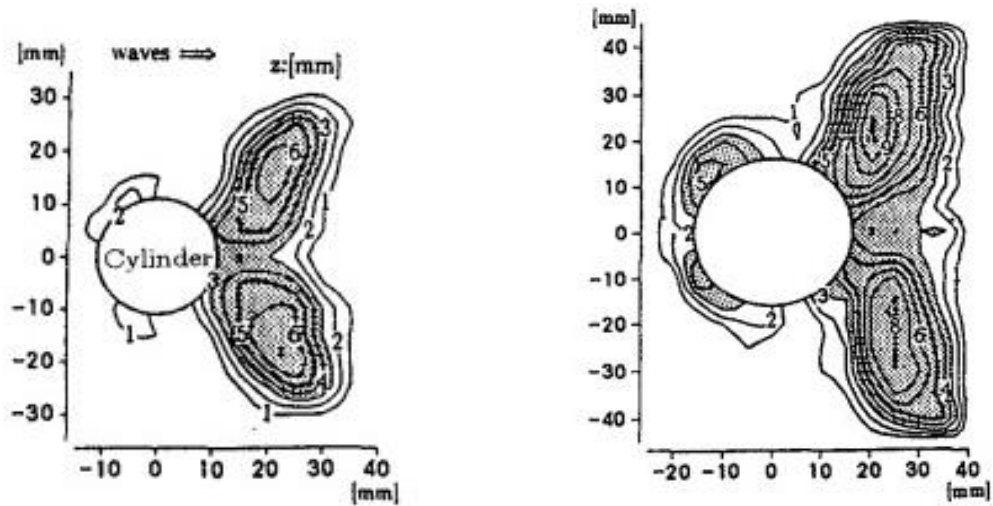
The parameters that influence the scour depth for waves-alone cases are the wave period, wave orbital velocity, and pier diameter. The wave orbital velocity depends on parameters like wave

height, water depth, etc. (Qi and Gao 2014). For current-only cases, the scour depth increases with the flow velocity (Mostafa and Agamy 2011; Sumer and Fredsøe 2001). It may seem that since both wave-alone and current-alone scenarios cause scours, their combined effect should be more severe than their individual effects, and that is true when the waves and currents are co-directional. When they come from opposite directions, however, the effects of the waves counteract the effects of the current. Since the scour is much deeper in current-alone than in waves-alone scenarios, waves coming from the opposite direction cannot completely nullify the effect of the current. Therefore, their combined effect creates scour that is deeper than in the waves-only cases but shallower than in the current-only cases (Jensen et al., 2006; Raaijmakers and Rudolph 2008).

2.4. Scour Hole Shape and Size

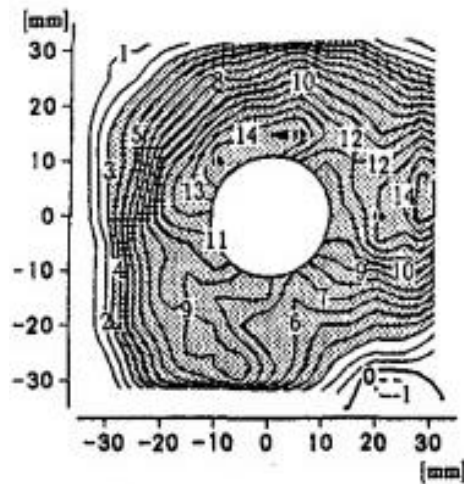
Determining the shape and size of the scour hole is an integral part of the engineering design of piers, as they vary under different flow conditions. Eadie and Herbich (1986) studied the shapes of scour holes for wave-only cases and found that after the shape is fully developed, it looks like a radially symmetric frustum of an inverted cone. Under these conditions, the scour hole initiates at the sides of the pier and some deposition may be found at the upstream and downstream sides. Kobayashi and Oda (1994) investigated local scour around vertical cylinders for wave-alone cases and revealed that the area of wave-induced scour holes is around 3-4 times the diameter of the pier. They classified scour beds into three types: twin-horn-shaped, transient-shaped, and cone-shaped (**Figure 2.3**) and presented a relationship between the development of these shapes with an increase in the Keulegan-Carpenter (KC) number (defined in Section 2.5.2). The scour hole type was investigated in sand materials collected from five different places in Japan (**Figure 2.4**), and their results showed that low KC numbers correspond to the twin-horn shaped scour profile. With increasing KC , the shape first changed to a transient shape, then to a cone shape. These results

were based on small-scale flume measurements. Chen and Li (2018) conducted large-scale flume experiments and observed similar shapes for lower KC numbers: however, for large KC numbers they observed shapes that were different from those reported by Kobayashi and Oda (1994). One explanation could be that the larger flume in Chen and Li's experiments (2018) resulted in non-linear waves being generated. Another could be the strong sidewise waves that were produced in Chen and Li's (2018) experiments.



(a) Twin-horn

(b) Transient



(c) Cone shape

Figure 2.3. Typical wave-induced scour hole (Kobayashi and Oda 1994)

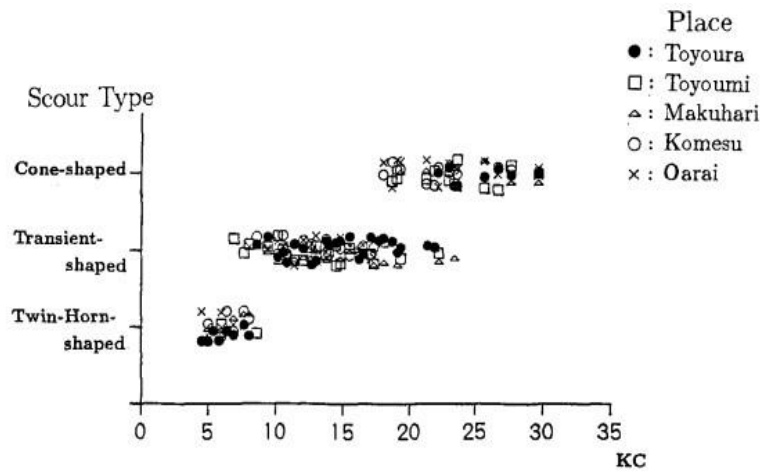


Figure 2.4. Relationship between the scour type and KC number in different sand samples collected from five places in Japan (Kobayashi and Oda 1994)

Melville and Coleman (2000) investigated the size of scour holes for the current-only condition and found that they were between two and five times the diameter of the pile. Eadie and Herbich (1986) also performed several experiments on the current-only and combined wave and current cases and found that the shapes of the scour holes were similar and resembled inverted truncated cones. Their experiments showed that sediment was carried further downstream by the combined wave and current scenario than by the current-only, and the size of the scour hole was equal to or larger. Niedoroda and Dalton (1982), however, espoused that the size and shape of a scour hole in the combined waves and current scenarios are smaller than that developed by a steady current alone. Armbrust (1982) mentioned that the shape of the scour hole pattern for wave-only cases is not as prominent as those for the current-only cases, as the pattern becomes irregular due to the wave particle orbital motion. With steady currents-only and combined wave-current flows, the scour hole is horizontally semicircular and vertically inverted cone shaped around the pier, and the dune-like deposit on the downstream or wake region is somewhat trapezoidal or irregular in shape (Kawata and Tsuchiya 1988; Williams et al., 2021). The downstream accretion starts at a distance

from the pier. It depends on the velocity of the flow if there will be a scour hole immediately downstream of the pier or not. Even if there is, it is smaller than the scour depth upstream of the pier (Li et al., 2020). The shape of the scour hole observed during the equilibrium stage of scour is formed at the initial stage and does not change with time, regardless of the type of scour (Kobayashi and Oda 1994).

Das et al. (2014) investigated local scour around circular piers for current-only cases and provided empirical equations for calculating the depth, length, width, area, and volume of the scour. Equations that can be used to estimate the scour's length and width are given below:

$$\frac{l_{se}}{D} = \{-1.333 \times \left(\frac{y}{D}\right) + 8.012\} \times \left(\frac{S}{D}\right) \quad (2.1)$$

$$\frac{W_{se}}{D} = \{0.558 \times \left(\frac{y}{D}\right) + 4.801\} \times \left(\frac{S}{D}\right) \quad (2.2)$$

where S , l_{se} and, W_{se} are the maximum equilibrium scour depth, length, and width respectively. D is the pier diameter, and y is the water depth. A comparison between their observed values and the values obtained from Equations 2.1 and 2.2 showed that the observed values of scour lengths were within a $\pm 30\%$ deviation interval of the predicted values, and the observed values of scour widths were within $\pm 10\%$ deviation interval (Das et al., 2014).

2.5. Mechanism and Prediction of Scour

Flow structure and scour phenomena occur around piers due to the pressure gradient (Guo et al., (2012) that results from the flow-structure interaction, flow-sediment interaction, or sediment-structure interaction. When the flow meets the pier, both the vertical and horizontal pressures change and depending on how deep the flow is, a hydrostatic and kinetic component of the total energy may change along the vertical plane of the pier and initiate scour. Boundary layer flows

are also created along the upstream pier perimeter and help create the wake vortices responsible for the downstream scour. The flow-structure interaction initiates the interaction between the flow and sediment as well. After the encounter between the flow and the pier, the direction of the flow changes and begins to interact with the sediment at the bottom of the pier. The horseshoe and wake vortices work together to push the sediment downstream from the bottom of the pier, and the scour grows backward, to the stagnation point from both sides. The sediment moving downstream with the strong vortices eventually decays into small eddies, resulting in a deposition. Sediment-structure interaction is not as important as the flow structure or flow sediment interactions, but if the grain size to pier diameter ratio is significant, it may affect the scour process. In practice, however, this value is very insignificant and does not affect the scour process.

Scour can be predicted in several ways that can be broadly grouped into four categories: analytical methods, physical modeling, numerical modeling, and field observations. Analytical and numerical approaches analyze the physics of the scour mechanism to derive a formula, and physical modeling and field observation approaches use experimental data to perform regression analysis and describe the scouring process. These approaches are referred to as empirical or semi-empirical approaches and are widely used in engineering projects. Several equations can be used to predict scour caused by waves-alone, current-alone, or wave-current combined conditions. The scour mechanism in these flow conditions and the equations that have been developed to predict it are discussed in this section.

2.5.1. Scour Around Piers in Current-alone Cases

Local scour around cylindrical piers in riverine conditions has been studied extensively over a long period of time. The riverine condition represents the current alone cases. As discussed above, the interaction between the flow and the pier creates a complex flow field that creates multiple

vortices. The main features of this flow field are surface rollers at the water surface on the upstream side of the bridge pier and downflow at the upstream side of the pier in the vertical plane, horseshoe vortices created as a result of the interaction of the downflow and bedform, and wake vortices on the downstream side of the pier (**Figure 2.5**). The downflow, the horseshoe, and the wake vortices are the main reasons for scour around a pier under a steady current. In their research in 2014, Qi and Gao observed that the horseshoe vortex, including the downflow, is the most dominant. As the scour hole grows, the vortex also rapidly grows and strengthens.

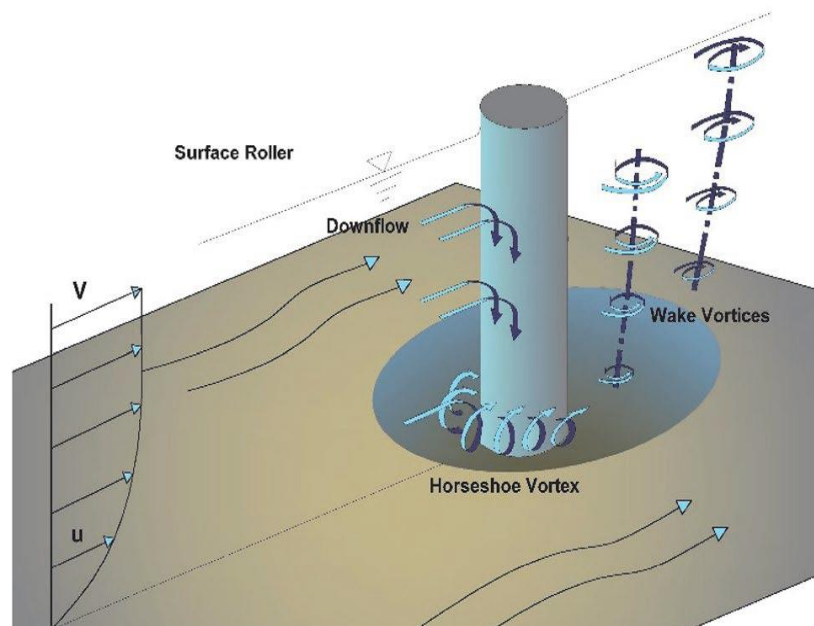


Figure 2.5. Scour pattern around a cylindrical bridge pier in current-only condition (Akhlaghi et al., 2020)

Predicting the equilibrium scour depth is an important factor in the design of a bridge, and multiple equations have been developed to predict it around piers in a steady current. An equation developed at Colorado State University and later revised by Richardson and Davis (2001) was published in the Hydraulic Engineering Circular No. 18 (HEC-18) and is applicable for both clear-water and live-bed scour.

$$\frac{S}{D} = 2.2 \times \left(\frac{y}{D}\right)^{0.35} \times Fr^{0.43} \quad (2.3)$$

Here, S is the equilibrium scour depth, D is the pier diameter, y denotes flow depth, and Fr is Froude number $Fr (= \frac{v}{\sqrt{gy}})$. Another scour prediction equation was provided in a subsequent edition of the HEC-18 circular.

$$\frac{S}{y} = 2.0 \times K_1 \times K_2 \times K_3 \times \left(\frac{D}{y}\right)^{0.65} \times Fr^{0.43} \quad (2.4)$$

where K_1 , K_2 , and K_3 are correction factors accounting for the pier nose shape, angle of attack of the flow, and bed condition. According to the study conducted by Wilson (1995), the scour depth may be estimated using Equation 2.5.

$$S = 0.9 \times D^{0.6} \times y^{0.4} \quad (2.5)$$

Lacey's (1929) method for estimating scour depth for loose bed alluvial rivers is given by Equation 2.6 in which q is the discharge intensity in $m^3/meter$ and f is the silt factor – calculated by $f = 1.76\sqrt{d_{50}}$, where d_{50} is the median size of bed material in mm.

$$S = 1.34 \times \left(\frac{q^2}{f}\right)^{\frac{1}{3}} \quad (2.6)$$

As per Raudkivi and Ettema's (1983) experimental results, scour in a steady current is heavily dependent on the particle size distribution, mean particle size of bed sediment, flow depth, and size of the pier. Many researchers have developed envelope curves based on their experimental results, but since there can be many unknown factors in field conditions, most experts recommend following a conservative design approach. For example, the effect of moving ripples on the equilibrium scour depth is not yet fully understood, and there could be other factors that would skew the prediction. For these reasons, it is recommended that a deeper scour be assumed for design purposes (Zanke et al., 2011).

2.5.2. Scour Around Piers in Wave-alone Cases

The main difference between scour induced only by waves and scour induced only by currents is the timescale. The duration of the wave-induced effects on the mean flow field is shorter than that of either tidal or non-tidal currents (Douglass and Webb 2020). The differences between the scour mechanism in riverine and coastal environments are discussed in FHWA-HEC25 (Douglass and Webb 2020). Flow in wave-dominant environments is unsteady and multi-directional; it swings back and forth around the pier, disrupting the development of the boundary layer, which is formed fully in current-induced flows. The Keulegan-Carpenter number (KC) is a dimensionless number that is used to express the relative magnitude of the flow and structure length scales and is one of the main parameters that defines the scour during waves-alone conditions. The KC is:

$$KC = \frac{U_m T}{D} \quad (2.7)$$

In this equation, U_m is the maximum wave-induced velocity, T is the wave period, and D is the pier diameter. U_m can be calculated using the following equation:

$$U_m = \frac{\pi H}{T} \times \left(\frac{1}{\cosh[kd]} \right) \quad (2.8)$$

In Equation 2.8, k is the wave number, and it can be calculated by $k = \frac{2\pi}{L}$. When $KC < 1$, the wave field and pier interactions dominate the scour process. When $6 < KC < 1000$, the vortex shedding is the only governing factor of the scour process. For $KC > 1000$ the scour process reaches an equilibrium value due to the quasi-steady nature of the flow relative to the size of the pier (Douglass and Webb 2020). The flow field around a pier under wave-alone conditions for $6 < KC < 100$ is shown in **Figure 2.6**. The wave actions stir up the bed materials, and sediment particles are eventually carried away from the vicinity of the pier. As a result, a net scour hole is formed around the pier in each half cycle of the waves (Gazi et al., 2019). The depth of the scour hole due

to waves is small compared to those created by the current-alone or by the combined waves and current; the maximum depth may reach up to 1.3 times the pier diameter (Douglass and Webb 2020). According to Sumer et al. (1993), scour depth is expected to be insignificant for KC numbers below 6, as there is no vortex shedding or horseshoe vortex creation. Local velocities caused by the apparent contraction of the streamlines are also insignificant in this condition.

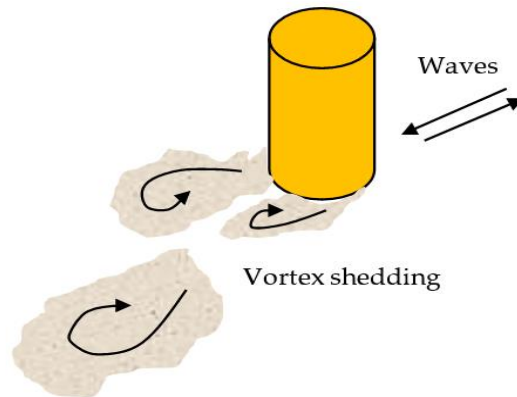


Figure 2.6. Flow field around a pier under wave-alone conditions ($6 < KC < 100$) (Gazi et al., 2019)

Sumer et al. (1993) proposed a formula to determine scour depth in wave-induced, live-bed conditions when $KC > 6$:

$$\frac{S}{D} = 1.3 [1 - e^{-0.03(KC-6)}] \quad (2.9)$$

where D is the pier diameter. Later Kobayashi and Oda (1994) proved, with their experimental data, that Equation 2.9 is valid for predicting scour in clear-water flow as well. The performance of Equation 2.9 was initially examined for regular waves by Sumer and Fredsøe (2001), but Zyserman and Fredsøe (1988) later concluded that it can also be used for irregular waves if the KC number is calculated using Equation 2.10.

$$KC = \frac{U_{rms} T_{wp}}{D} \quad (2.10)$$

where U_{rms} is the orbital velocity ($= \sqrt{2} \sigma_U$ in which σ_U is the root-mean-square (RMS) value of the orbital velocity U at the bottom), and T_{wp} is the wave period. Preperneau et al. (2009) argued that Equation 2.9 is not efficient in predicting scour under irregular waves; therefore, Zanke et al. (2011) conducted further study and showed that wave-induced scour depends on both the KC number and the relative water displacement. In support of their statement, they proposed Equation 2.11 for predicting scour depth:

$$\frac{S}{D} = 2.5 \left(1 - 0.5 \frac{u_{cr}}{u} \right) x_{\text{rel}} \quad (2.11)$$

where u_{cr} is the critical inflow velocity for the initiation of sediment motion, u is the orbital velocity, x_{rel} is the relative water displacement ($= x_{\text{eff}}/(1+x_{\text{eff}})$), x_{eff} is the effective water displacement calculated using Equation 2.12:

$$x_{\text{eff}} = 0.03 \left[1 - 0.35 \left(\frac{u_{cr}}{u} \right) (KC - 6) \right] \quad (2.12)$$

In this equation, U is the mean velocity in steady currents, and U_{cr} is the critical velocity. The critical velocity is calculated as $U_{cr} = 1.4 \left(2 \times \sqrt{\frac{\rho_s - \rho_w}{\rho_w} g d_{50}} + 10.5 \frac{\nu}{d_{50}} \right)$, where ρ_s denotes the density of sediment, ρ_w is the density of water, and ν is the kinematic viscosity of water.

All the methods discussed above are focused on wave-induced flow regimes having a KC number above 6. According to Douglass and Webb (2020), $KC < 1$ is typically observed due to the interaction of the wave field with very large piers. In most of the published literature, the KC range of 1 to 6 has been ignored. Webb and Matthews (2014) conducted a study on this transition zone, collected 256 waves scour data for different KC numbers, and proposed a set of equations that covers a KC range from 0.1 to infinity. **Figure 2.7** illustrates the curve that best fits all the scour

data collected. The best fit equation and a more conservative upper bound equation suggested from this analysis are given below:

$$\frac{S}{D} = 1.3 \left[1 - 0.99 \times e^{-0.022(KC-0.1)} \right] \quad (\text{Best fit}) \quad (2.13)$$

$$\frac{S}{D} = 1.3 \left[1 - 0.97 \times e^{-0.05(KC-0.1)} \right] \quad (\text{Upper Estimate}) \quad (2.14)$$

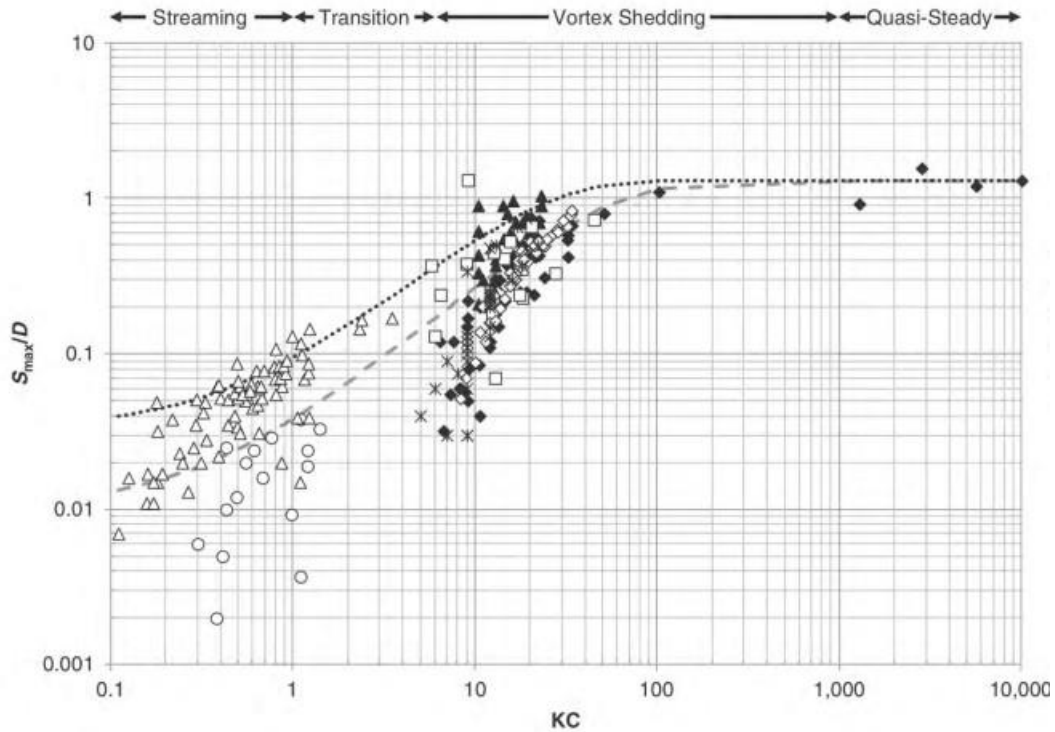


Figure 2.7. Wave-induced local pier scour depth ratio (S_{\max}/D) as a function of Keulegan-Carpenter number (KC) (Webb and Matthews 2014)

2.5.3. Scour Around Piers Under Combined Waves and Current

Waves and currents co-exist in lacustrine environments, and the mechanism of bridge scour in these environments is much more complex than in riverine locations. Bridges located in lacustrine areas may be impacted by waves, tides, tsunamis, and hurricanes, and the scour occurs because of the interaction between the bridge piers and abutments with currents and waves. Since waves are more capable of lifting sand and currents are more capable of carrying it, in a wave-current

combined environment, sand is picked up by waves and then transported by the current. But it is not just the superimposition of their capacity to lift and carry sediment that makes it unique. The primary reasons that make combined scour unique are: 1) there is no distinct flow from an upstream source of sediment, 2) flows are unsteady and multi-directional, 3) waves complicate the scour processes, and 4) large surge/stage events do not always produce large velocities. The crossings are categorized as tidally influenced, tidally dominated, and tidal bridges, and they may experience large storm-induced currents and wind-induced waves. The complex interaction between the waves and the current leads to a particular boundary layer and velocity profile that is different from the current-alone and wave-alone environments. Sumer and Fredsøe (2001) introduced the parameter U_{cw} which represents the ratio of wave and current components in wave-current flows

$$U_{cw} = \frac{U_c}{U_c + U_m} \quad (2.15)$$

in which U_c is the undisturbed current velocity at the distance $y = D/2$ from the bed representing the near-bed current velocity ($D =$ pier diameter) and U_m is the maximum value of the undisturbed orbital velocity at the bottom, just above the wave boundary layer. The value of U_{cw} varies between 0 and 1, with $U_{cw} = 0$ and 1 representing the wave-alone and current-alone conditions. The scour depth and shape with the combined wave and current cases approach its steady current values when $U_{cw} \geq 0.7$ (Sumer and Fredsøe 2001). A scour hole around a pier that is caused by waves alone is not very deep but becomes larger under the combined effects of waves and the current (Kawata and Tsuchiya 1988; Sumer and Fredsøe 2001). In fact, the study conducted by Qi and Gao (2014) showed that the maximum depth of the scour hole caused by the combined waves and current action was greater than the linear sum of those separately created by wave-alone and current-alone. These results were confirmed by Eadie and Herbich (1986). The current and wave interaction in the vicinity of a pier is schematically shown in **Figure 2.8**. Sumer and Fredsøe (2002)

proposed an empirical equation for equilibrium scour depth under combined waves and current, based on data they obtained in 2001:

$$\frac{S}{D} = \frac{S_c}{D} [1 - e^{-A(KC-B)}] \quad \text{for } KC \geq B \quad (2.16)$$

where S_c is the scour depth for current alone case and parameters A and B can be calculated as $A = 0.003 + 0.75U_{cw}^{2.6}$ and $B = 6e^{-4.7U_{cw}}$, respectively. This equation is only applicable for live-bed conditions and for a KC number from 4 to 26. For lower KC numbers, Raaijmakers and Rudolph (2008) developed Equation 15:

$$S_{eq} = 1.5D \times \tanh\left(\frac{h}{D}\right) \times K_w \times K_h \quad (2.17)$$

In this equation, $K_w = \left(\frac{h_p}{h}\right)^{0.67}$ is a correction factor that accounts for wave effects, where h_p denotes the pier height and K_h , the correction factor for piers that are partly submerged under water, $= 1 - e^{-c}$ and $C = 0.012KC + 0.57KC^{1.77}U_{cw}^{3.76}$. Chen and Li (2018) used these equations to predict scour for cases of combined waves and current and compared them with their experimental results. They found that the equations provided reasonable estimations of scouring for larger KC numbers but underestimated scour for cases with lower KC numbers.

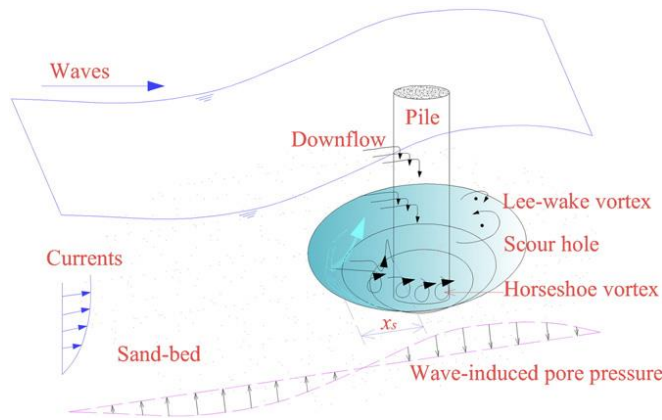


Figure 2.8. Flow field around a pier under combined wave-current conditions (Qi and Gao 2014)

From the discussion above, it is clear that the scour mechanism for wave-only and current-only cases has been studied extensively. The scour mechanism of combined wave and current conditions, however, is not as well understood.

It needs to be noted here that the studies mentioned above were conducted on scenarios of co-directional waves and current or waves propagating perpendicular to the current. None of them investigated scenarios of waves propagated against the current. Mostafa and Agamy (2011) investigated cases of waves against currents and concluded that when the wave direction is against the direction of current, the resulting scour depth is less than that caused by currents only.

2.6. Timescale

The scour area and depth grow around the pier with time. The depth varies depending on the flow field and size of the pier. It takes longer to reach the equilibrium scour depth in clear water scour conditions. Kumar et al. (1999) observed the change in scour depth of current-only cases and concluded that equilibrium is reached when the scour depth changes less than one mm in three hours. Mia and Nago (2003) considered that equilibrium was reached when the scour depth did not increase more than 5% D (D is the pier diameter) in 24 hours. Bozkus and Yildiz (2004) and Karimi et al. (2017) suggested that scour depth reaches its equilibrium state after two hours. Liang et al. (2019) conducted a comparative study and found that it takes several weeks to reach the total scour depth. Within the minimum duration of two hours suggested above, approximately 50% of the total scour was reached; in 2.5 days, 77% of the scour was reached; and in less than 10 days, 90% of the total scour was reached.

Sumer et al. (1992) proposed Equation 2.18 for wave-alone cases:

$$S_t = S \left[1 - e^{\left(-\frac{t}{\bar{t}}\right)} \right] \quad (2.18)$$

In this equation, S is the equilibrium scour depth, and T is the time period required to reach the equilibrium scour depth. It can be obtained by drawing a tangent to the slope of the $S_t(t)$ curve at $t = 0$ (Figure 2.9).

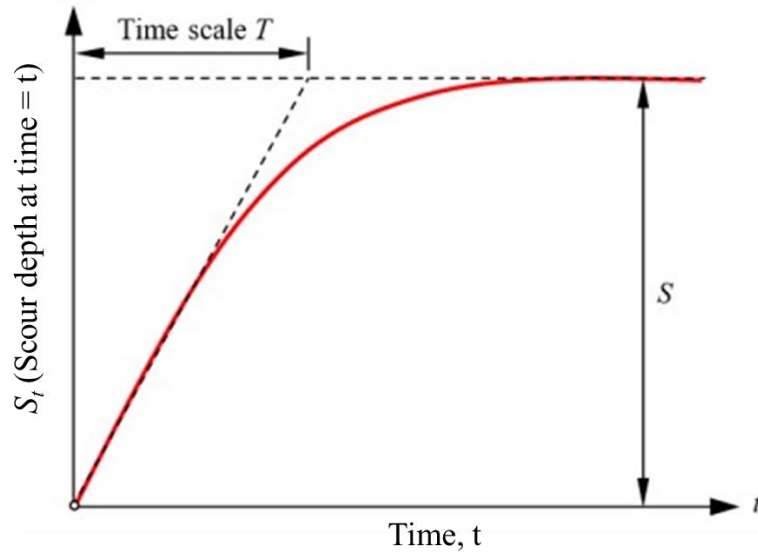


Figure 2.9. Evolution of equilibrium scour depth, $S_t(t)$ at time t

Chen and Li (2018) examined the validity of the formula proposed by Sumer et al. (1992) for a wave and current combined case and found the results reasonably acceptable. Qi and Gao (2014) also investigated the temporal evolution of scour depth for wave and current combined cases and suggested that to reach equilibrium scour in small-scale laboratory experiments, the test has to be run for several days. Nevertheless, according to their observation, the maximum scour depth was less than 1.2 times the scour depth observed within 100 minutes. They also proposed a formula for determining scour depth development with time. Most of these studies did not consider the direction of wave propagation with respect to the direction of the current. Mostafa and Agamy (2011) conducted wave and current combined experiments where the wave direction was opposite to the current direction and observed that the depth of the scour did not increase after three hours.

2.7. Employing Particle Image Velocimetry (PIV) to Visualize Flow Around Piers

Particle image velocimetry (PIV) is a method that is widely used for acquiring two- and three-dimensional hydraulic information. A basic setup requires an illuminating light source (laser), tracer particles, and a high-speed camera that captures a time series of images in a specified illuminated area to analyze and produce a detailed representation of the flow field. Fluid properties, such as velocity vectors, streamlines, and shear stresses, over a given duration, can be obtained using this method. Its use was initially limited to laboratory experiments, but the introduction of a Large-Scale PIV (LSPIV) has overcome this limitation. It can now be used to investigate flow fields in large areas at field conditions and has proven highly efficient at providing a better understanding of different hydraulic phenomena, especially in and around hydraulic structures such as bridges, culverts, and guide-vanes used in stream restoration. Several researchers (e.g., Huang et al., 2014; Lin et al., 2003; Ozturk et al., 2010; and Schanderl et al., 2017) have used PIV for conducting scour experiments, and an attempt was made in this study to use it to investigate the flow field around a pier in the streamwise horizontal plane.

2.7.1. Typical Flow Structure Around a Cylindrical Pier

When an encounter occurs between the flow and a structure, the direction of the flow changes both vertically and horizontally, creating surface rollers, downflow, horseshoe vortices, and wake vortices. Wake vortices are created in a horizontal plane downstream of the structure. For wave-alone cases, the flow around the cylinder is oscillatory, and the creation of wake vortices and vortex shedding characteristics depend on the Keulegan-Carpenter (KC) number. Sumer and Fredsøe (2006) performed extensive research on flow structures around cylinders in oscillatory flow and their findings on changes in the flow pattern change with increasing KC value are provided in **Figure 2.10**.

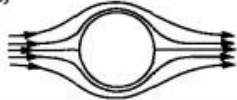
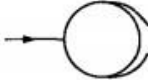
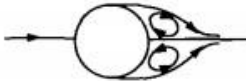
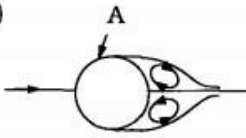
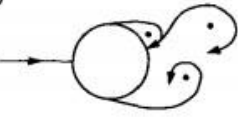
a)		No separation. Creeping (laminar) flow.	$KC < 1.1$
b)		Separation with Honji vortices.	$1.1 < KC < 1.6$
c)		A pair of symmetric vortices	$1.6 < KC < 2.1$
d)		A pair of symmetric vortices. Turbulence over the cylinder surface (A).	$2.1 < KC < 4$
e)		A pair of asymmetric vortices	$4 < KC < 7$
f)		Vortex shedding	$7 < KC$ Shedding regimes

Figure 2.10. Type of flow regime around a circular cylinder in oscillatory flow at different KC numbers (Sumer and Fredsøe 2006)

2.7.2. PIV Components

PIV is a non-intrusive velocity measurement tool that can capture instantaneous velocity fields in a defined flow region. It uses light-reflecting tracer particles, an illuminating light source, and a high-speed camera to capture the velocity profile within a certain time frame. As light-reflecting particles are not naturally present in a flow, it must be seeded with tracer particles that are as dense as water and small and light enough to move with the flow velocity (Brossard et al., 2009). The light source used to illuminate the tracer particles is usually a laser sheet. Using an appropriate

lens, the laser ray is converted into a sheet and projected into the region of interest. A typical PIV setup is shown in **Figure 2.11**.

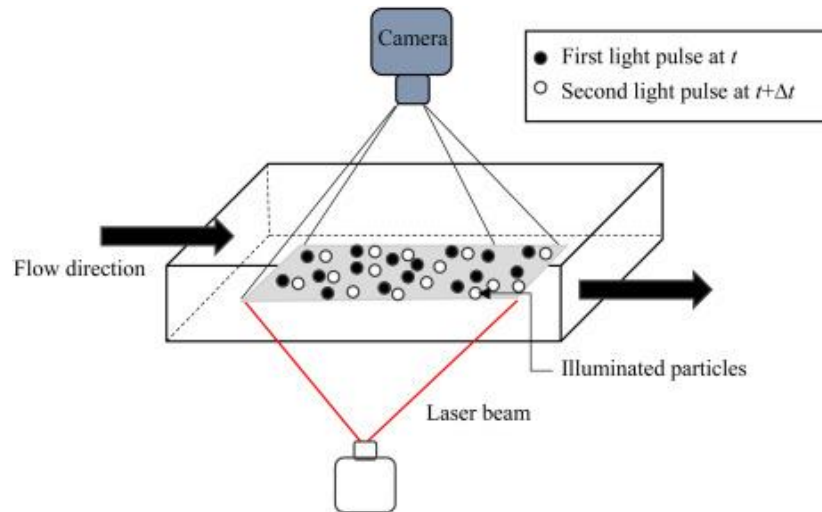


Figure 2.11. Typical arrangement for particle image velocimetry (PIV) (Sim and Fane 2017)

After capturing the required images, cross-correlation analysis is performed to track the particles as they move from one frame to another. This analysis extracts the displacement of the particles within a known time interval, which helps to determine the direction and velocity of the particles on a point-by-point basis. Determination of the flow field allows for calculating the vorticity and shear stress (Horst, 2009; Unsworth, 2015). The main advantages of PIV are that it is non-intrusive technology that does not affect the flow field; it does not need to be calibrated; it is not affected by atmospheric parameters, such as temperature, humidity, etc.; and it performs efficiently despite adverse flow conditions (Hassan et al., 2020). Conventional PIV imaging technique has a limited field of view; therefore, its application is limited to measuring velocity fields of areas up to several square meters in laboratory flumes (Lloyd et al., 1995; Ettema et al., 1997).

2.7.3. Application of PIV for Visualizing Flow Field Around Piers and Scour Holes

Unger and Hager (2007) were the pioneers of using PIV to investigate flow characteristics around sediment-embedded bridge piers. They utilized PIV to observe the internal flow features around circular bridge piers both in vertical and horizontal planes and explored the velocity and vorticity properties around the pier. Ensuring optical visualization while using PIV can be challenging since it requires the use of transparent material and sediment is not transparent. They met the challenge by assuming that the structure of one-half of the channel flow was identical to the other half and placed a semicircular plexiglass pier at the glassed channel sidewall to ensure optical access into the scour hole.

Williams et al. (2019) used PIV to conduct three types of experiments to investigate flow around a submerged cylinder with local scour protection: flow around a submerged cylinder, flow around a submerged cylinder with a vertical plate and flow around a submerged cylinder with a horizontal base plate. All the measurements were taken in the vertical plane, the mean streamwise velocity was measured using PIV, and the shear layers were identified for all three experiments. These measurements helped identify the efficacy of employing a vertical splitter plate and a horizontal base plate as scour protection techniques for a submerged cylindrical pier. Williams et al. (2022) further extended their research on this topic by investigating the flow-altering capacity of these countermeasures around the cylindrical pier. Reynold shear stress distribution was investigated using PIV and compared for all three cases.

Williams et al. (2021) also investigated emergent circular cylinders using PIV and compared their mean velocity distribution and vector fields in the streamwise vertical plane with submerged cylinders. Although almost no difference was observed in the scour depth, the scour width and length of the submerged cylinder were larger than that of the emergent one. Some erosion was also

observed on the top of the primary deposit, and the PIV images revealed increased mean streamwise velocity at the top of the submerged cylinder. They assumed that this was caused by the separation of flow at the top and was the reason for the increased erosion at the top of the primary deposit and larger scour length and width.

Gautam et al. (2019) conducted a study to investigate flow and turbulence characteristics around both simple and complex piers. They used a commercial PIV system to collect velocity data around the piers for three Reynolds numbers and investigated flow characteristics such as mean flow, shear stress, velocity, vorticity, turbulent kinetic energy, and power spectra. Since no sediment bed was prepared, visual access was not an issue in their study. The flume bed and sidewalls were made of Perspex glass to ensure optical access to the PIV system.

CHAPTER 3

METHODOLOGY

3.1. Introduction

The two main components of this study are investigating the size and shape of scour holes around cylindrical piers under different flow conditions in a laboratory flume with a sediment bed, and studying the flow structure around cylindrical piers, using PIV in the streamwise horizontal plane. Extensive data were collected under different flow conditions for both setups. The experimental runs were carried out in a controlled environment in the University of Texas at Arlington Fluid Mechanics and Hydraulic lab.

3.2. Experimental Flume

A plexiglass flume with dimensions of 4.9 m (16 ft) length, 0.3 (1 ft) width, and 0.5 m (1.5 ft) depth and a maximum flow capacity of 200 gpm was utilized to acquire the experimental data for this study. A sediment bed was prepared and installed in the flume. Pumps recirculated the water and generated a current. Since the flume was not capable of handling sediment transport, the sediment bed was designed in such a way that a clear-water flow regime in the flume (no general bed erosion) in ensured. This setup ensured that even if the sand moved, it would stay inside the flume and would not enter the sump. The slope of the flume was capable of being adjusted within a range of -5% to 15% but was fixed at 0.03% to ensure a clear-water flow regime. An adjustable tailgate at the downstream end of the flume was used to control the water surface elevation for different experimental scenarios, and a wave generator was installed just upstream of the tailgate.

A flow straightener and a wave absorber were installed near the inlet. A schematic diagram of the flume is shown in **Figure 3.1**.

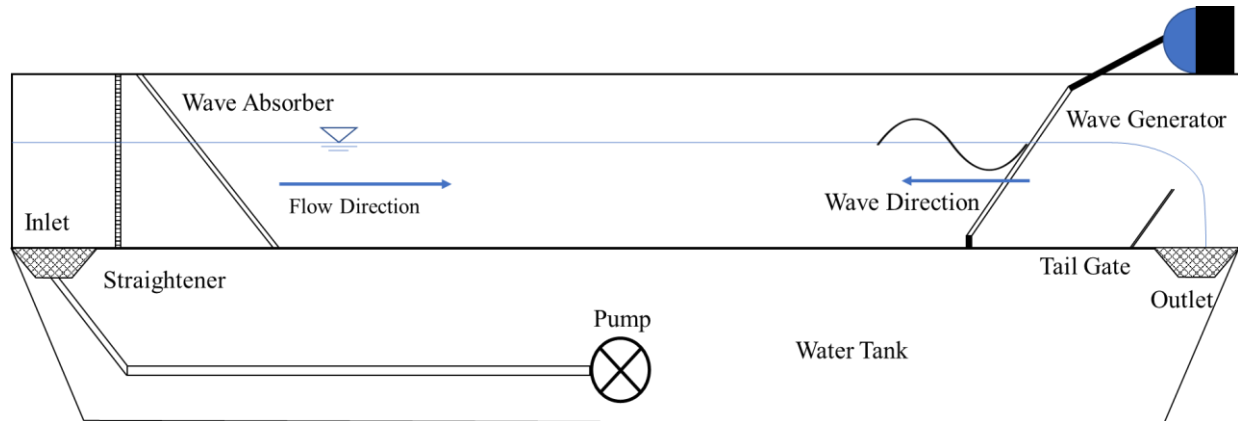


Figure 3.1. Schematic diagram of the experimental flume (not to scale)

3.3. Pier Models

Cylindrical piers with two different diameters ($D = 19$ mm and 50 mm) were used to observe how the dimensions of the pier affect the flow structure and size and shape of scour hole. The pier models are shown in **Figure 3.2**. Flow blockage was a consideration in selecting the piers' diameter, and to reduce this effect, the blockage ratio D/b (b : flow width) was always kept below 0.2, following the findings of Williams et al. (2021) and Li et al. (2020). The 50 mm pier was a hollow glass cylinder, and the 19 mm pier was a solid acrylic plexiglass rod. It was assumed that the piers' material does not affect the shape of the scour. Both piers were more than 0.3 m (12 inches) high to ensure that the pier was not fully submerged during the experiments and not too tall to block the view of the camera installed above the flume to capture the movement of the flow around the pier. If the piers had been submerged, it would have been difficult for the PIVLab software to analyze the flow, especially when the flow included waves causing back and forth movement of the seeded particles. Other than being emergent or submerged, the height of the pier typically does not have much effect on the scour. The pier was installed 2.5 m downstream of the

flume entrance, and a flow straightener was installed at the flume entrance to ensure that the flow was fully developed when it reached the pier. A picture of the flow straightener is provided in

Figure 3.3.



Figure 3.2. The 19 mm and 50 mm piers used in this study

3.4. Flow Scenarios

Experiments under different flow conditions were performed to investigate the flow structure and scour pattern around the piers. Three flow scenarios (wave only, current only, and wave and current combined) were developed in the flume to replicate the scour mechanism of riverine, coastal, and lacustrine environments.

3.4.1. Waves-alone Experiments

Regular waves were produced by a flap-type wave generator located at the downstream end of the flume. A sloped, porous steel-type wave absorber was installed at the opposite end to absorb the

wave reflection. When the waves-alone experiments were ongoing, the outlet of the flume was kept closed; the pumps were turned off after the desired water depth was achieved. The wave generator was connected to a speed controller (**Figure 3.3**) with a lever arm. The controller had a range of 0 to 100 rpm. At 100 rpm, the flume shook, which affected the wave propagation; consequently, the maximum speed of the wave generator was kept below 90 rpm. The mean water depth varied from 15 to 26 cm, and the wave height for this range of flow depth varied from 5.8 to 9.1 cm. Vertical graduated tapes attached to the flume and pier walls were used to measure the height of the waves and depth of the flow.

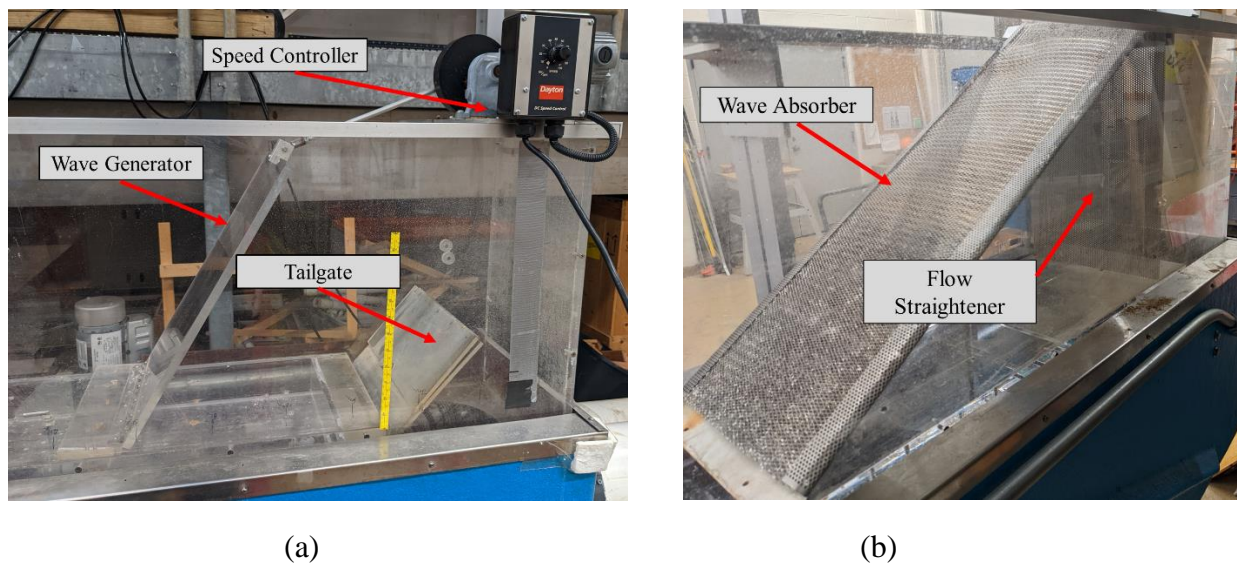


Figure 3.3. (a) Side view of the wave generator connected to the speed controller, with lever arm installed near the flume outlet; (b) wave absorber and flow straightener near the flume inlet

3.4.2. Current-alone Experiments

The current in the flume was produced by a pump that recirculated the water, and a honeycomb flow straightener was installed near the inlet to remove eddies generated within the inlet area and to develop a unidirectional flow (**Figure 3.3b**). No flow in the transverse direction was observed. The mean depth of the flow varied from 10.2 cm to 15.2 cm, and the depth and velocity of the flow

changed with the flow rate. The methods that were used to measure the different flow parameters are discussed in **Section 3.5**.

3.4.3. Wave and Current Combined Experiments

In the experiments where both waves and a current were present, the direction of the wave was opposite to the direction of the current. It affected the flow structure and scouring process around the pier differently than co-directional waves and current would have. The velocity component of the combined wave and current flow covered a rather small range since, similar to the wave-alone experiments – it was the flow depth that varied. Using similar flow parameters in different flow conditions helped compare the results of scour depth, shape, and size. The wave generator flap had to be modified to introduce the wave with the current component since the generator was at the opposite end of the flume inlet and blocked the flow recirculation by preventing the water from reaching the outlet. To address this issue, the wave generator flap was attached to the top of two 1.5-inch wood spacers to ensure an opening below the wave generator and allow the water to recirculate (**Figure 3.4a**). Due to the opening at the bottom, with the same water depth, the wave generator could produce a shorter wave height than it did during the waves-only experiments.



(a)

(b)

Figure 3.4. (a) Modification to the wave generator flap to run wave-current experiments, (b) modified wave generator in action

3.5. Measurement of Flow Parameters

The different scenarios developed in the flume required that a number of flow parameters be measured. For the wave-alone experiments, the wave height, wave period, and water depth were measured; for the current-only experiments, the flow rate, flow velocity, and flow depth were measured; and for the wave and current combined cases, all of the above-mentioned parameters were measured. The following section discusses the procedures that were followed to measure these parameters.

3.5.1. Flow Rate Measurement

The orifice method was used to measure the discharge supplied by the recirculatory pumping system. Two manometers that were attached to the wall of the flume showed the difference in the head before and after the orifice, from which the flow rate was calculated. The flume's two built-in pumps had a capacity of 100 gpm each, hence when both pumps were working at their full capacity, approximately 200 gpm of flow rate could be achieved.

3.5.2. Velocity Measurement

The continuity equation was used to calculate the depth-averaged velocity, and the point velocity upstream of the pier was measured at the beginning of each experiment, using a three-dimensional Acoustic Doppler Velocimeter (ADV) to validate the calculation. (**Figure 3.5**). The velocity was recorded upstream of the pier to ensure that the flow was not impacted by the presence of the pier. From ADV data, it was also observed that the transverse and vertical velocities were nearly zero.



Figure 3.5. Acoustic doppler velocimeter (ADV) used to measure the velocity

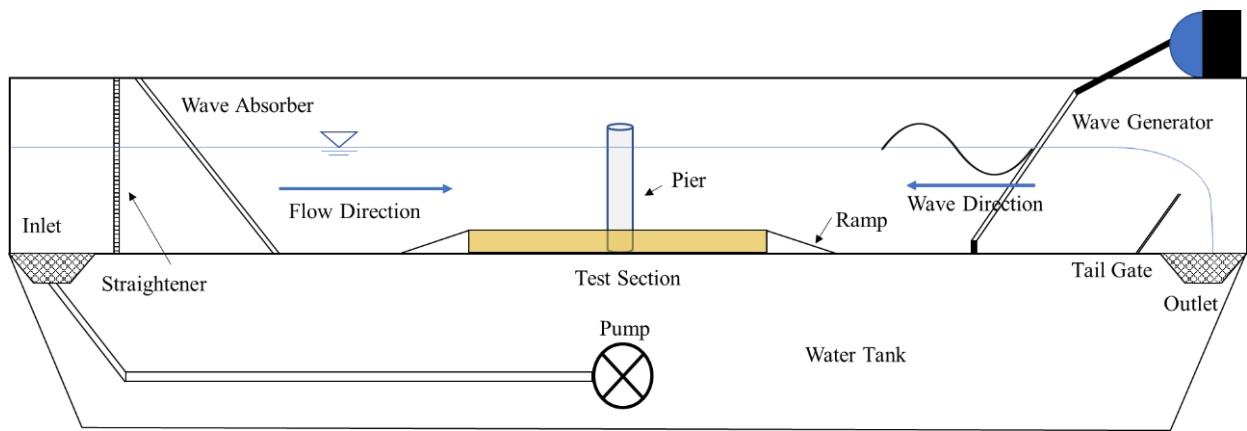
3.5.3. Flow Depth Measurement

Two methods were used to measure the flow depth. A point gauge was mounted upstream of the pier, and readings were taken when the tip of the needle of the point gauge touched the surface of the sand bed or bottom of the flume. Then the height of the point gauge was adjusted, and another reading was taken when it touched the surface of the water. The water depth was calculated from the difference between the two readings. To double-check the reading of the point gauge, measuring tapes with an accuracy of $1/16^{\text{th}}$ of an inch (1.16 mm) were affixed to the flume wall. They were useful for observing the upstream and downstream water depth and indicating whether any slope correction was required. Water depth measurements were taken at the center of the flume and the side of the flume wall at several locations upstream and downstream of the pier. It was

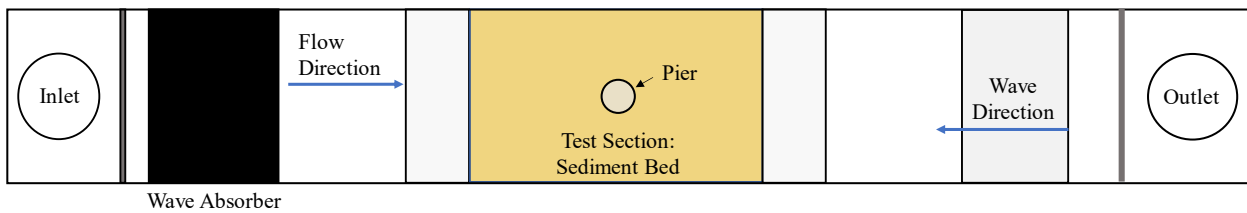
estimated that an error up to ± 0.002 m could occur. The flow depth could be adjusted using the tailgate situated at the downstream end of the flume.

3.6. Preparation of the Sediment Bed

The sediment bed was designed to ensure a clear-water regime in the flume. The size of the sediment particles was selected in such a way that the flow could not initiate movement in the bed and a clear water condition was maintained; only the sediment near the cylinder moved, due to turbulence activities caused by the presence of the pier. As the flow undulation only occurs near the cylinder, the clear water conditions help to identify the flow characteristics. **Figure 3.6** shows the schematics of the experimental setup with a sediment bed.



(a) Section View



(b) Plan View

Figure 3.6. Schematic of the laboratory flume and sediment bed

3.6.1. Determination of Sediment Size

The first step in designing the sediment bed was to determine the sediment size most favorable for all the experiments to ensure that the flow conditions developed in the laboratory, other than the secondary flow near the cylindrical pier, could not move the sand from the sediment bed. This study intended to investigate scour in non-cohesive soil. Different combinations of water depth, bed slope, and sediment diameters were considered, and the relative flow intensity Y/Y_{cr} for each combination was calculated. In this quantity, Y is the mobility number expressed by:

$$Y = \frac{\tau_0}{(\rho_s - \rho_w)gd_{50}} \quad (3.1)$$

where ρ_s is the sediment density, ρ_w is water density, and d_{50} is median sediment diameter. τ_0 is current related bed shear stress ($=gRS$, where S is the bed slope, R is the hydraulic radius, and g is gravitational acceleration).

Y_{cr} is the value of Y at the critical stage (stage of inception of sediment transport). It is a function of the roughness Reynolds number and can be obtained from the Shields diagram. The Shields diagram used to calculate the mobility number is provided in **Appendix A**.

When Y is higher than Y_{cr} , the sediment moves with the flow, and it was observed that the mobility number increased with the slope increment. A flow intensity Y/Y_{cr} below 1 indicates that the flow shear stress is smaller than the critical shear stress of the sediment with a certain diameter; therefore, the flow would not cause erosion and sediment transport in the flume. Y/Y_{cr} between 0.7 and 1.2 is considered a transitional zone, so the flow parameter and sediment size used in all the experiments maintained a maximum Y/Y_{cr} of 0.7. The sediment size calculated based on this criterion was between 0.8 mm to < 2 mm. Calculation of sediment size is provided in **Appendix A**.

3.6.2. Sieve Analysis

Since it was determined that sediment between 0.8 and 2 mm would ensure a clear water flow regime, a large volume of silica sand was passed through several sieves (#14, #16, #18, #20, and #25) to extract sand with a uniform gradation within this range. (**Figure 3.7**). The sediment size was kept as small as possible with the mildest slope achievable in the laboratory flume (0.00032). Since little sand was retained on #25 sieve and below, the sand retained on #18 and #20 sieves were mixed to prepare the sediment bed. The sand had a median diameter of $d_{50} = 0.95$ mm and geometric standard deviation of $\sigma_g = d_{84}/d_{16} = 1.27$. The d_{84} and d_{16} represent particle sizes at 84% and 16% finer, respectively, which, according to the ASTM standards D2487, can be classified as uniformly graded sand (ASTM, 2006). The results of the sieve analysis are shown in **Appendix B**.

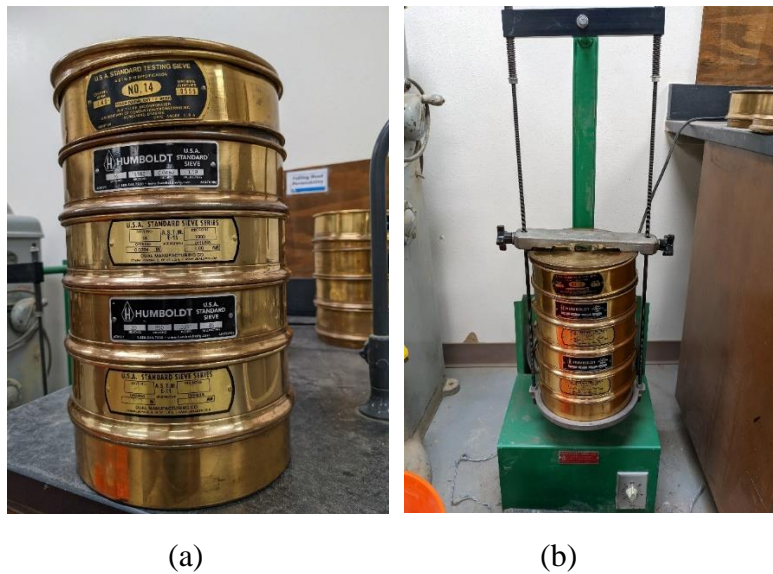


Figure 3.7. (a) #14, #16, #18, #20, and #25 sieves were used to obtain uniform sand for the sediment bed, (b) sieve test apparatus

3.6.3. Sediment Bed

The sediment bed was prepared after the sieve analysis had been completed and the correct amount and size of sand had been extracted. The dimensions of the sediment bed were 1.2 m long, 0.3 m wide, and 5 cm deep (**Figure 3.8**). Initially, the sediment bed was designed for a 19-mm pier. Equilibrium depth for the 19-mm pier was calculated using the appropriate equations discussed in Chapter 2, and the sediment bed was designed accordingly. But later, it was decided to test a 50-mm pier, to check the effect of the pier size on scour. Since the sediment bed was not designed for the 50 mm pier, the scour reached the bottom of the sediment bed when the flow velocity was high enough. Since this study's focus was on the scour hole shape and size (length and width), the sediment bed was not re-designed with the equilibrium scour depth of the larger pier; the experiments were simply stopped whenever the scour reached the bottom of the bed. The cylindrical pier was installed in the middle of the sediment bed, and four vertical graduated tapes were attached to the wall of the pier at 0° (upstream side), 90° (left to the flow direction), 180° (downstream side), and 270° (right to the flow direction) to measure the depth of the scour hole. The length of the sediment bed was selected to ensure that the pier was far enough away from the edges of the sediment bed that it would not be affected by any flow disturbance that might occur at these locations. Two ramps with 1V:6H slopes were attached to either side of the sediment bed to create a smooth transition between the flume and sediment beds (**Figure 3.8**). Once the sediment bed was installed in the flume, the sieved sand was placed in it in three approximately equal lifts and was manually compacted. The sediment bed was kept under water for 24 hours so that the gaps between the sand particles would fill in and the soil would be uniformly hydrated. Prior to each run, the sediment in the test section was carefully leveled with a trowel. At the upstream end of sediment recess, even after providing a ramp, some flow turbulence occurred, and local scour

was observed (**Figure 3.9**). The scour and ripple effects were only observed within the first few inches of the edge of the sediment box and did not affect the local scour around the pier. Once each experimental run was completed, the flow rate was gradually reduced, then turned off to avoid any disturbance to the sediment bed.

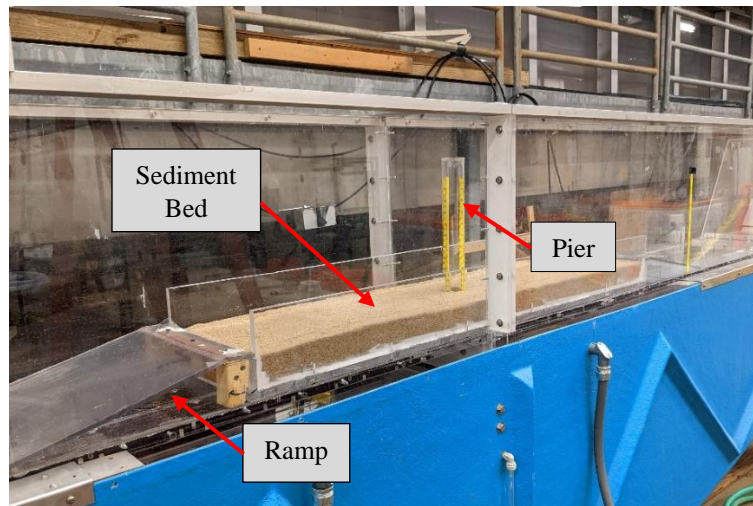


Figure 3.8. Sediment bed for the scour experiments

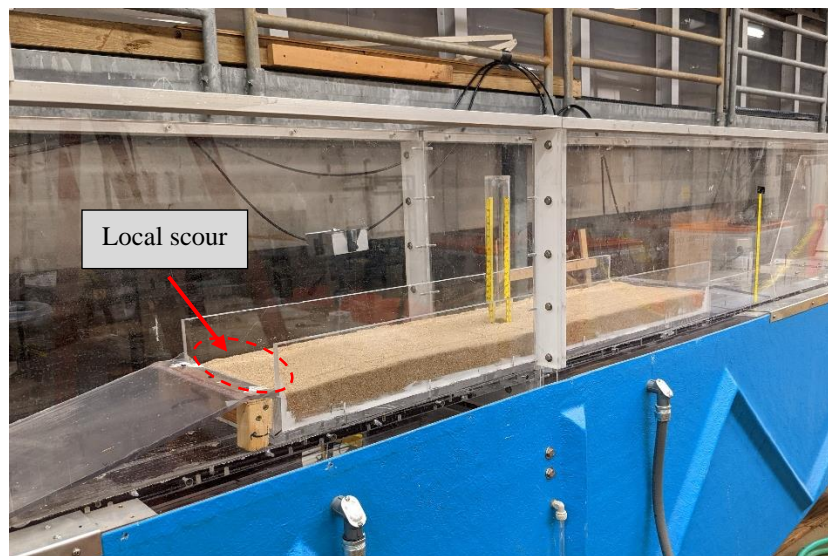


Figure 3.9. Local scour observed near the edge of the sediment bed

3.7. PIV Setup and Data Acquisition

An inexpensive PIV setup was developed for this study to investigate the flow characteristics around piers. The system included a laser light, a GoPro camera, and seeding particles. As the flume wall was built of plexiglass and the cylindrical piers were also transparent, there was no visual obstacle for the laser. **Figure 3.10** shows a schematic of the experimental setup with the PIV system. From multiple trials, it was observed that the flow patterns were identical on both sides of the cylinder and the geometry of the scour holes was reasonably symmetric about the pier symmetry plane. For this reason, all of the results of the PIV tests only show half of the setup.

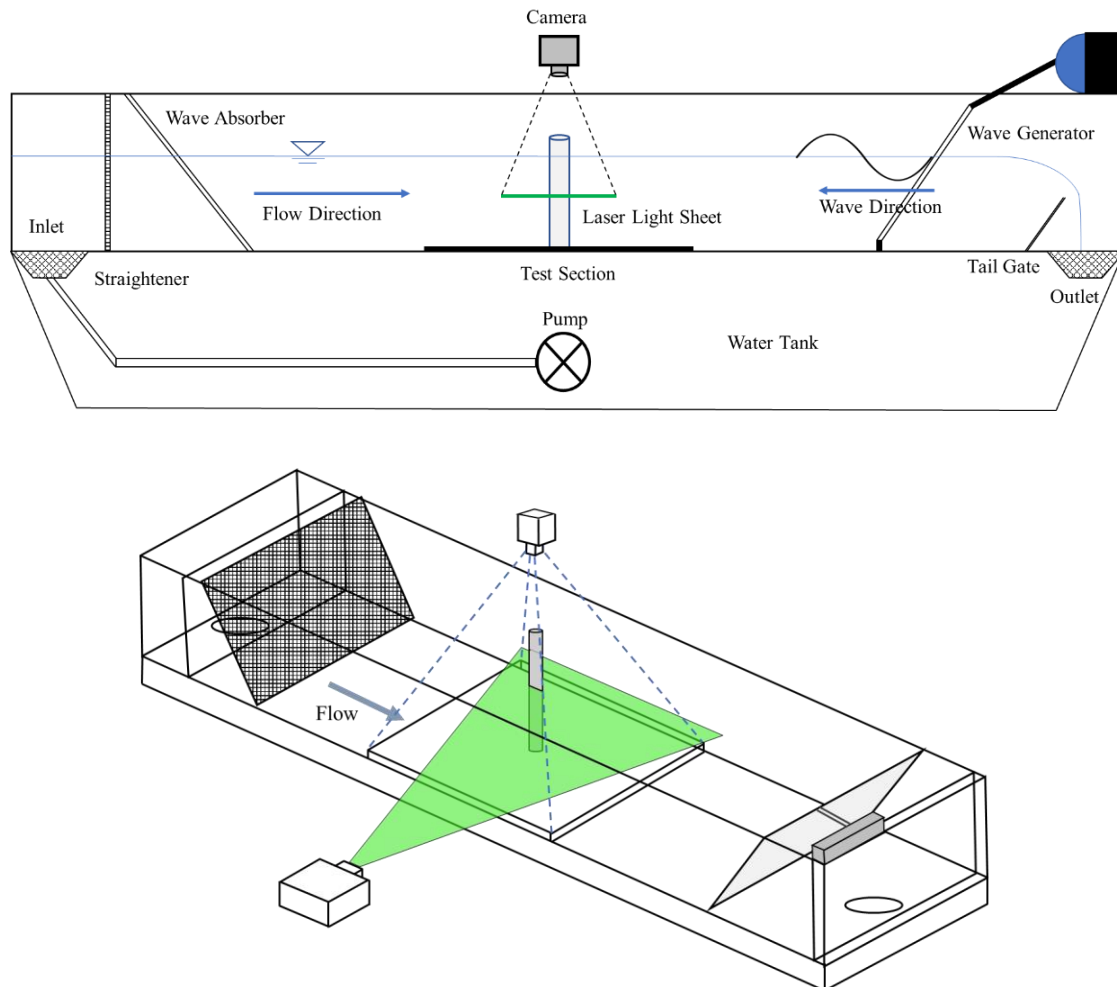


Figure 3.10. Experimental arrangement for the particle image velocimetry

3.7.1. Laser

A 1-watt powered green laser was mounted on a tripod and connected to a cylindrical lens to produce a 2 mm thick laser sheet at the test section. The laser and the flume were approximately 0.6 m apart. Measurements were obtained in the horizontal plane.

3.7.2. Seeding Particles

Silver-colored particles with a mean diameter of 47 microns and density of 2.04 g/cm^3 were used as seeding material to illuminate the flow field for the laser sheet, and the fluid motion around the pier was investigated by tracing the path of the particles. The settling velocity of the silver particles estimated from Stokes' law was about 0.125 cm/s, which was smaller than the average flow velocity produced in this study.

3.7.3. Camera

A high-speed photography method is required for an efficient PIV system, and in this study, the flow images were captured with GoPro Hero 5 action video camera that was set to 28 mm focal length and narrow field of view (FOV) to achieve the maximum frame rate (240 Hz with a pixel resolution of 1280×720). The average acquisition time was kept at 15 seconds, which corresponds to 3600 images. The camera was mounted on a tripod above the test section to provide a view of the horizontal plane.

3.7.4. Post Processing (PIVLab)

PIVLab, a MATLAB extension tool, was used as a post-processing tool in this study to extract the velocity data by analyzing the video recordings captured during the experiments. It analyzed two consecutive frames to trace the distance that different particles traveled at times t_0 and $t_0 + \Delta t$, and from this data calculated the velocity of the laser-illuminated area. The particle displacement was calculated for a group of particles by evaluating the cross-correlation of many small sub-images

(interrogation areas). Details of the PIVLab working procedure can be found in Thielicke and Stamhuis (2014). Slight discontinuities and scatter in the distribution of the velocities were observed in the processed images because of the variability in intensity along the laser sheet. Williams et al. (2021) faced the same issue with the laser while working on their PIV setup.

3.8. Flow Conditions

A total of 19 experiments were performed, 6 for waves-alone, 6 for current-alone, and 7 for the combined wave-current scenario. Two piers were used under different water depths. In the wave-only condition, the height of the waves changed with a change in the water depth. In the current-only experiments, the flow depth and flow velocity changed with a change in the flow rate. The same changes occurred during the combined wave and current experiments. After several trials for each flow condition, it was observed that the current-only scenario was the most aggressive of the three flow conditions and caused the deepest scour hole. **Table 3.1** summarizes the test conditions of all the experiments.

Table 3.1. Test Conditions for Flume Experiments (Waves propagating opposite to the current direction)

Pier	Flow Condition	Water Depth, d (cm)	Wave Height, H (cm)	Wave Period, T (s)	Wave Length, L (cm)	KC	Flow Rate, lit/s	Flow Velocity, m/s	Time Duration, min	
50 mm	Waves Only	15.2	7.6	0.70	70.5	2.31	-	-	600	
		17.8	8.4	0.70	72.5	2.16	-	-	600	
		20.3	9.1	0.70	73.8	1.96	-	-	600	
	Current Only	10.2	-	-	-	-	4.8	0.157	120	
		12.7	-	-	-	-	6.6	0.174	12*	
		15.2	-	-	-	-	12.4	0.272	3*	
	Waves and Current Combined	15.2	6.4	0.68	67.3	1.81	7.0	0.153	120	
		17.8	7.0	0.72	75.9	1.91	8.6	0.161	120	
		20.3	7.6	0.70	73.8	1.65	9.7	0.158	120	
		25.6	8.2	0.70	75.4	1.24	12.4	0.161	120	
	19 mm	Waves Only	15.2	7.6	0.72	73.6	6.39	-	-	600
			17.8	8.4	0.72	75.9	6.07	-	-	600
20.3			9.1	0.72	77.5	5.56	-	-	600	
Current Only		10.2	-	-	-	-	4.9	0.159	120	
		12.7	-	-	-	-	6.7	0.174	120	
		15.2	-	-	-	-	12.4	0.272	120	
Waves and Current Combined		15.2	5.8	0.69	68.9	4.53	7.2	0.157	120	
		17.8	7.0	0.72	75.9	5.04	8.6	0.161	120	
		20.3	7.6	0.72	77.5	4.68	9.7	0.159	120	

*Note: The duration of two of the current-only experiments were less 2 hours. With the 50 mm pier, the scour reached the bottom of the bed before the end of experiment when the velocity was high enough, and the experiments were stopped.

CHAPTER 4

RESULT AND DISCUSSION

4.1. Introduction

The results from the laboratory experiments and their analysis are presented in this chapter. As mentioned earlier, this study is divided into two main areas. The geometry of the scour hole around the circular pier was investigated from the experiments using the sediment bed, and flow characteristics around those piers were observed using PIV.

4.2. Scour Hole Geometry Subject to Different Flow Conditions

Scour patterns in three types of flow environments were investigated: current-alone, waves-alone, and combined waves and current. The shape and size of the scour hole grew rapidly for the current-only and combined waves and current scenarios and showed a definite pattern within the short period of two hours that the experiments were run. For the wave-alone cases, a longer duration (approximately 10 hours) was needed to obtain a definite pattern. The results from the experiments are presented in the following section.

4.2.1. Waves-alone Cases

The sand particles at the bottom of the pier moved very little during the wave-alone experiments; therefore, the experiments were run for a longer time to reach a stable scour pattern. The KC values for the designed experiments were quite low ($5.5 < KC < 6.5$ for the 19-mm pier and < 2.5 for the 50-mm pier). However, unlike the observation of Sumer et al. (1993), some scour was detected for wave-only conditions with KC values lower than 6. Maximum scour depth was observed on the sides of the pier. The width of the scour was measured perpendicular to the wave direction and the

length was measured parallel to the wave propagation direction. The test conditions and results for the wave-only cases are summarized in **Table 4.1**.

Table 4.1. Test Conditions and Results for Local Scour Around a Cylindrical Pier: Waves-alone Cases

Pier	Flow Depth, d (cm)	Wave Height, H (cm)	Wave Period, T (s)	KC	Maximum Scour Depth, (cm)	Width of Scour, (cm)	Length of Scour, (cm)
50 mm	15.2	7.6	0.70	2.31	0.4	3.6	9.4
	17.8	8.4	0.70	2.16	0.4	4.0	12.4
	20.3	9.1	0.70	1.96	0.3	4.6	15.9
19 mm	15.2	7.6	0.72	6.39	0.4	4.2	14.2
	17.8	8.4	0.72	6.07	0.35	4.0	12.4
	20.3	9.1	0.72	5.56	0.35	3.4	8.5

Typically, with a constant water depth, the KC number increases with increasing wave height, and results in a deeper scour hole. That is why different wave heights were generated in this series of experiments. Due to the limitations of the flume, the water depth had to be changed as well to adjust the wave height, which is inversely correlated to the KC number. The results showed that the scour depth increased with an increasing KC number, which supports the statement made by Sumer et al. (1993) that KC is one of the most relevant parameters that determine the scour depth in wave-only conditions. Since the wave-only cases were run for longer periods and the change of bed elevation around the piers was not significant, it was assumed that the scoured bed reached its equilibrium depth within that time. Below is a comparison of the equilibrium scour depth calculated from different scour depth prediction equations and the observed depth for the waves-alone case.

Table 4.2. Comparison of Calculated and Observed Non-Dimensional Equilibrium Scour Depth (S/D) for Waves-alone Cases

Observe and Calculated Scour Depth	KC					
	1.96	2.16	2.31	5.56	6.07	6.39
Observed Depth	0.064	0.078	0.09	0.184	0.179	0.211
Sumer et al. (1993)	-	-	-	-	0.003	0.016
Zanke et al. (2011)	-	-	-	-	0.04	0.038
Webb and Matthews (2014)	0.064	0.07	0.074	0.158	0.168	0.179

Sumer et al. (1993) and Zanke et al. (2011) suggested equations that are valid for KC values above 6 (Equations 2.9 and 2.11, respectively). Since there are no predicted scours for $KC < 6$ from these equations, those boxes are blank in **Table 4.2**. In two cases, when the KC was above 6, these two equations underestimated the scour depth, but the observed values and predicted depth of scour from Webb and Matthews’s (2014) equation (Equation 2.13) were similar.

For cases with a KC value below 6, some scour was observed at the lateral sides of the cylinder, with some deposition at the upstream and downstream sides. The scattered depositions, in which no definite pattern was observed, are indicated in **Figure 4.1a**. These results support Armbrust’s (1982) observation for waves-only cases. For cases with a KC value above 6, some scour pattern was observed that was close to the twin-horn shape described by Kobayashi and Oda (1994), but not as prominent as expected (**Figure 4.1b**). In Kobayashi and Oda’s (1994) experiments, the twin-horn shape was observed for KC values of 5-10. The KC values for the 19 mm pier in this study fell on the lower side of this range, which may be why a precise twin-horn shape was not observed for the wave-only scenarios. One contributing factor could be the size of sand particles used in the sediment bed. As the d_{50} was 0.95 mm, which is much bigger than the sediment sizes used in other studies that conducted the wave-alone experiments.

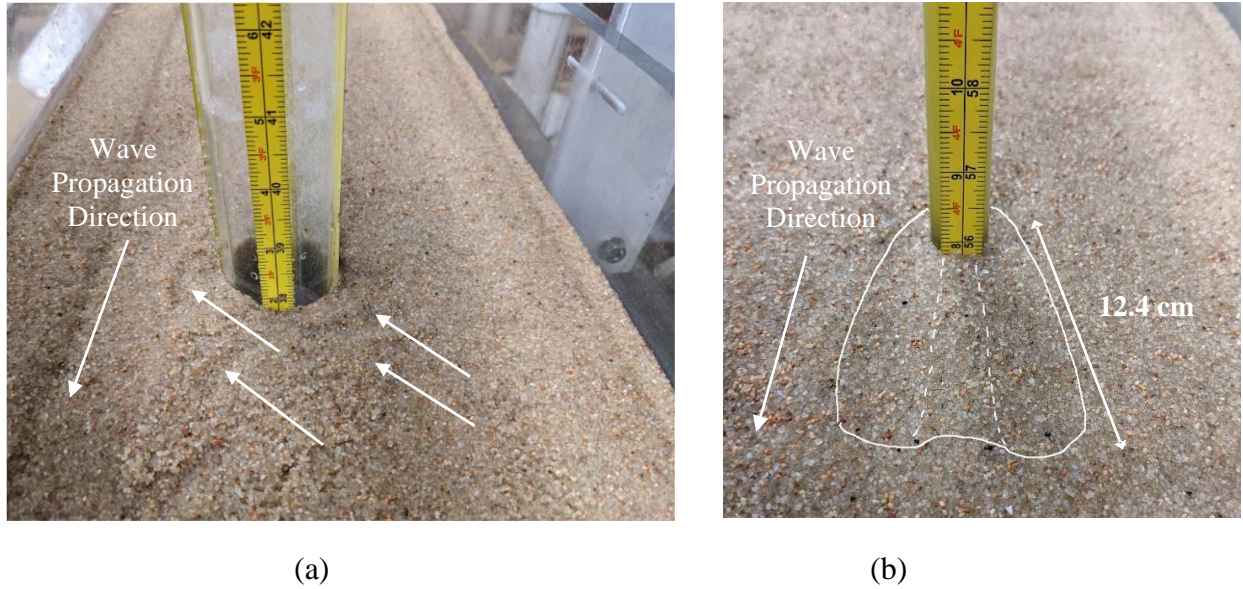


Figure 4.1. Scour under wave-only cases: (a) $KC < 6$ (50 mm pier), and (b) $KC > 6$ (19 mm pier)

Horseshoe vortices do not fully develop under wave-only conditions because of the thin bottom boundary layer and back and forth movement of the waves. According to Chen and Li (2018), flow contraction and wake vortices govern the scour process in wave-only conditions and produce this twin horn shape. The location of the maximum scour points around the pier for waves-only cases is provided in **Figure 4.2**, which shows that most of them were located on the sides of the pier, slightly downstream from the center of the pier in the direction of wave generation. The center of the pier was considered the origin in **Figure 4.2**, and all the measurements were taken with respect to this point.

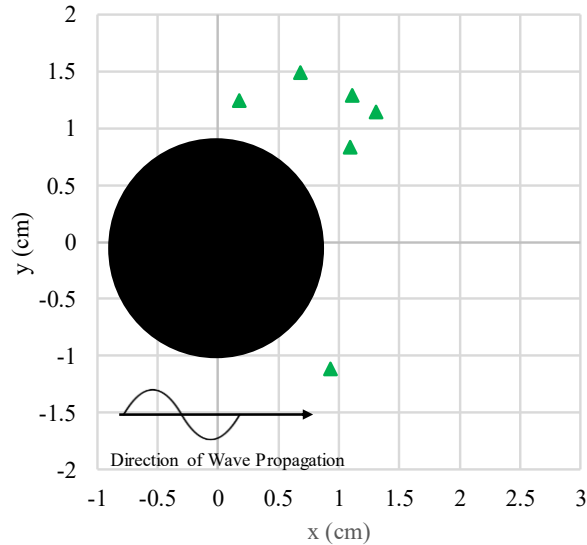


Figure 4.2. Distribution of maximum scoured points under waves-alone flow condition

4.2.2. Current-alone Cases

The current-alone cases were the most extreme of the flow conditions investigated. Six experiments were performed under different flow depths, flow velocities, and pier diameters. In two of those, the scour reached the bottom of the sediment bed much earlier than the two hours of the designed experiment, and once they reached the bottom, the experiments were stopped. All the scour holes under the current-alone conditions showed a clear geometric pattern. The maximum scour points for these cases were located at the front end (upstream side) of the pier. The width of scour hole was measured perpendicular to the flow direction, the distance of the edge of the scour hole from the upstream end of the pier, and the distance of the sediment deposition downstream was measured parallel to the flow direction. The test conditions and results for the current-only cases are summarized in **Table 4.3**.

Table 4.3. Test Conditions and Test Results for Local Scour Around a Cylindrical Pier: Current-alone Cases

Test No.	Pier	Flow Depth, d (cm)	Flow Velocity, (cm/s)	Max Scour, (cm)	Width of Scour, (cm)	Scour edge distance from U/S end of Pier, (cm)	From D/S end of the Pier		Max. Deposition Height, (cm)
							Total Deposition Distance, (cm)	Max. Deposition distance, (cm)	
1	50 mm	10.2	15.7	2.8	12.3	3.8	9.5	7.6	2.5
2		12.7	17.4	-	19.6	8.3	22.1	17.2	3.5
3		15.2	27.2	-	19.2	8.4	24.1	20.3	3.5
4	19 mm	10.2	15.9	1.9	8.4	3.1	8.6	7.3	1.3
5		12.7	17.4	2.0	9.1	3.9	13.6	10.5	2.1
6		15.2	27.2	2.4	13.5	5.4	53.3	26.7	1.4

Each of the geometrical parameters investigated increased in magnitude with a change in flow velocity. In Test 1 and Test 4, with a flow depth of 10.2 cm, after the initial scour was caused by the presence of the pier, the flow velocity was not strong enough to carry the sediment accumulated behind the pier further downstream. But that was not the case for the other two flow velocities investigated. The experiment duration was two hours. Since in two cases with the 50 mm pier, the scour depth reached the bottom of the bed earlier than the end of two hours, it was not possible to compare their geometry with the results of other experiments. With a flow velocity of 27.2 cm/s, the scour depth reached the bottom of the bed in only three minutes, and with a flow velocity of 17.4 cm/s, the scour reached the bottom of the sediment bed in twelve minutes. Due to the limited depth of the sediment bed, in all experiments, the scour hole would have reached the bottom of the sediment bed before reaching the equilibrium depth. For this reason, the equilibrium scour depth for the current-only experiments was extrapolated based on the observation made by Liang et al. (2019) that 45.8% of the equilibrium scour depth is reached within a period of two hours. The equilibrium scour depth was calculated using Equations 2.3, 2.5, and 2.6, and the results are compared in **Table 4.4**.

Table 4.4. Comparison of Observed Scour Depth with Calculated Values from Other Studies

Test No.	Observed and Calculated Equilibrium Scour Depth (cm)			
	Extrapolated Observed Depth	Richardson and Davis (2001)	Wilson (1995)	Lacey (1929)
1	6.1	6.4	6.0	7.2
2	-	6.9	6.5	9.0
3	-	8.5	7.0	13.6
4	4.1	3.4	3.3	7.3
5	4.5	3.6	3.7	9.0
6	5.3	4.5	3.9	13.6

From **Table 4.4**, it can be observed that the extrapolated observed scour depth values were much lower than the values predicted by Lacey’s (1929) equation, but the other two equations agree reasonably well with the extrapolated observed values, although both equations slightly underestimated the depth of scour hole. It must be kept in mind that the observed values were the extrapolated ones, and if the experiment duration had been longer, the final equilibrium depth could have been even closer.

Other features of the scour hole in the current-alone cases also agree well with the previous studies. The inverted truncated cone-shaped scour hole was observed in all the experiments performed. The distance of the downstream deposition varied with the flow velocity, and very little scour was observed downstream when the flow velocity was low. The shape of the primary deposit downstream resembled trapezoidal shapes, but when the velocity was high for the 19 mm pier, the sides of the deposits moved further downstream than the middle section and resembled two horns. The shape and size of the scour holes for the current-alone cases are presented in **Figure 4.3**, **Figure 4.4**, and **Figure 4.5**.

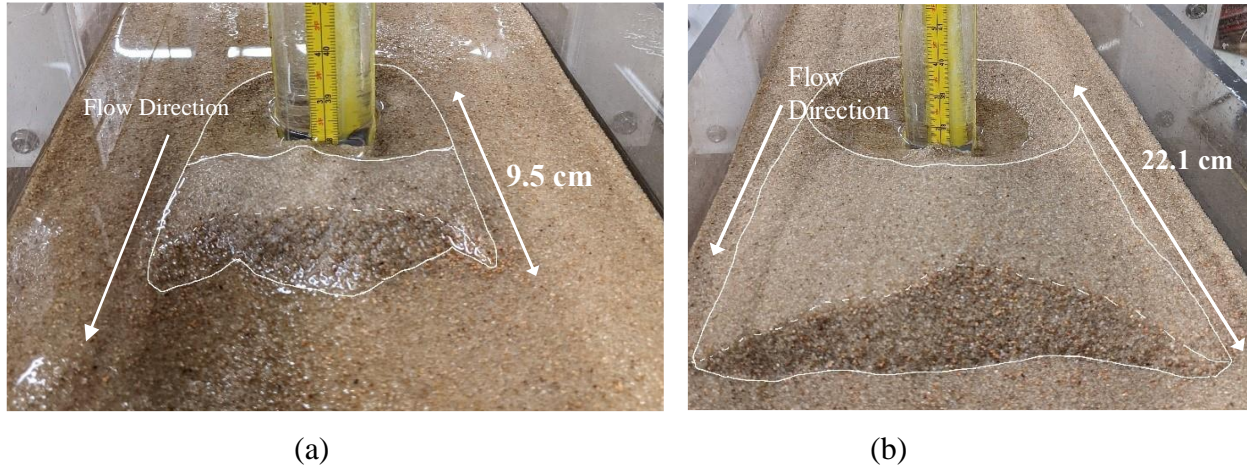


Figure 4.3. Scour around 50 mm pier in current-only experiments: (a) water depth = 10.2 cm, flow velocity = 15.3 cm/s; and (b) flow depth = 12.7 cm, flow velocity = 17.4 cm/s

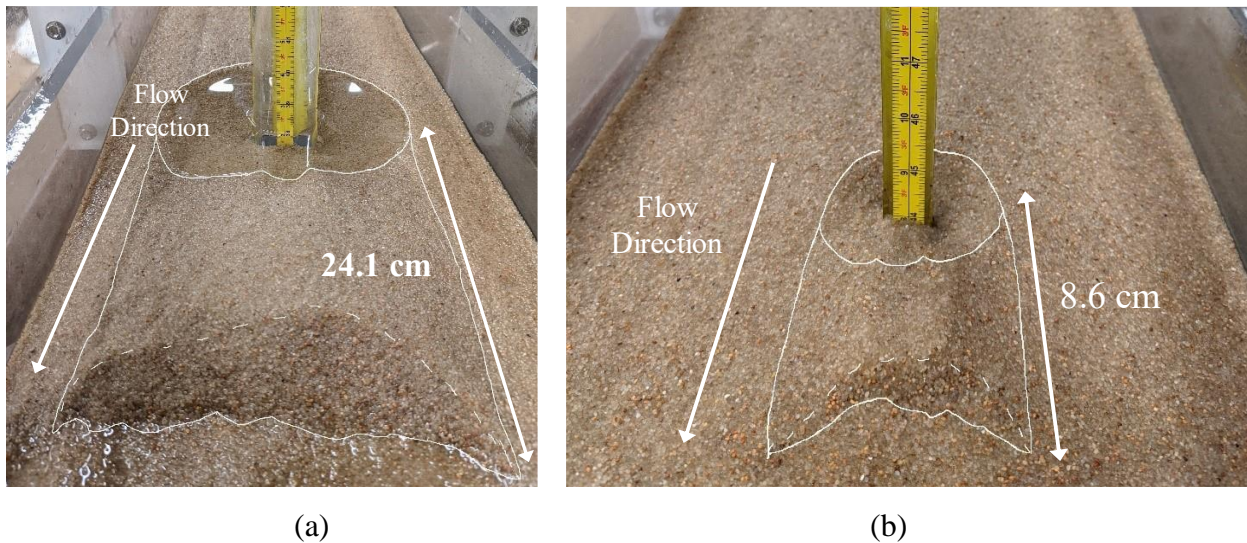
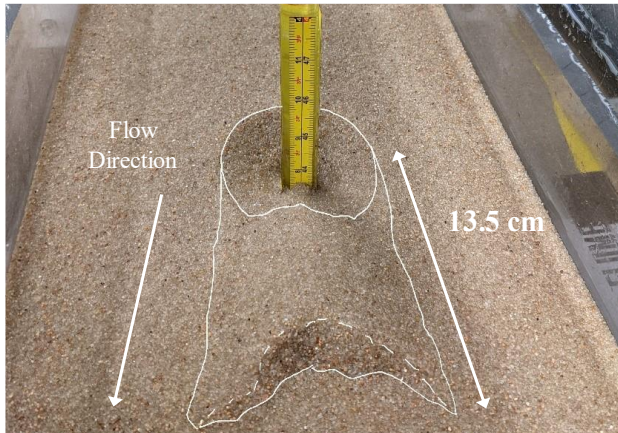
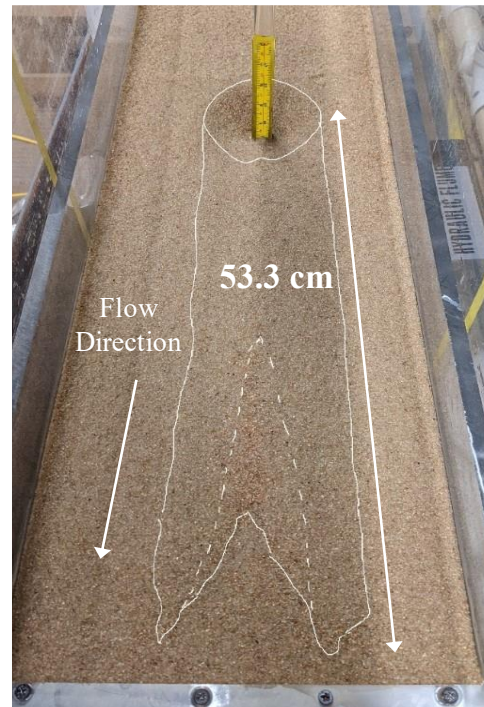


Figure 4.4. Scour around piers in current-only experiments: (a) 50 mm pier, water depth = 15.2 cm, flow velocity = 27.2 cm/s; (b) 19-mm pier, water depth = 10.2 cm, flow velocity = 15.9 cm/s

Unlike Test 3 (50 mm pier, water depth = 15.2 cm, flow velocity = 27.2 cm/s), Test 6 (19 mm pier, water depth = 15.2 cm, flow velocity = 27.2 cm/s) did not reach the bottom of the sediment during its runtime. It was the highest velocity investigated, and the deposition downstream of the pier moved further downstream very quickly; at the end of two hours, it had almost reached the downstream edge of the sediment bed **Figure 4.5b**.



(a)



(b)

Figure 4.5. Scour around 19 mm pier in current-only experiments: (a) water depth = 12.7 cm, flow velocity = 17.4 cm/s; and (b) water depth = 15.2 cm, flow velocity = 27.2 cm/s

4.2.3. Combined Wave and Current Cases

Seven scenarios were investigated for the combined wave and current cases. The direction of the flow was opposite to that of wave propagation. Water depths in these scenarios were similar to the wave-alone cases. Because of the small opening below the wave generator installed near the outlet of the flume, the flow depth was much higher than in the current-alone cases with the same flow rate. Because of this obstruction, it was not possible to achieve the velocity of the current-alone cases in this set of experiments. On the other hand, because of the opening below the wave generator, which allowed the recirculation of water during this set of experiments, the height of the generated waves was smaller than what was generated during the wave-alone experiments with the same water depth. As the wave height became smaller, all the KC values for the combined experiments were below 6 for both the 19- and 50-mm piers, and the scouring process was heavily

dominated by the current component. All the scour holes in these waves and current experiments showed a clear geometric pattern similar to the current-alone cases. The maximum scoured points were located on the upstream side of the pier, but the lateral sides had almost similar depths. The width of the scour hole was measured perpendicular to the flow direction. The distance between the edge of the scour hole from the upstream side of the pier and the distance of the sediment deposition downstream were measured parallel to the flow direction. The test condition and results for the wave-current combined cases are summarized in **Table 4.5**.

Table 4.5. Test Conditions and Results for Local Scour Around a Cylindrical Pier: Wave and Current Combined Cases

Test No.	Pier	d (cm)	U (cm/s)	U_m (cm/s)	U_{cw} (cm/s)	KC	Max Scour, cm	Width of Scour, (cm)	Scour Dis. U/S end of Pier, (cm)	From D/S end of the Pier		Max. Depos. Height, (cm)
										Total Depos. Dis., (cm)	Max. Depos. Dis. (cm)	
7	50 mm	15.2	15.3	13.4	0.53	1.8	2.1	13.6	4.9	14.0	9.21	1.11
8		17.8	16.1	13.3	0.55	1.9	2.3	16.4	6.0	23.4	16.51	1.75
9		20.3	15.8	11.8	0.57	1.6	2.0	14.5	4.6	21.3	14.29	1.43
10		25.6	16.1	8.6	0.65	1.2	2.6	17.6	4.8	14.9	12.85	2.06
11	19 mm	15.2	15.7	12.5	0.56	4.5	1.6	5.6	3.0	12.3	10.16	1.27
12		17.8	16.1	13.3	0.55	5.0	1.8	7.6	2.7	16.5	8.89	0.95
13		20.3	15.9	12.4	0.56	4.7	1.8	7.6	2.1	8.3	6.35	0.79

In the table above, U_c is the undisturbed current velocity, U_m is the maximum value of the undisturbed orbital velocity, U_{cw} is calculated from Equation 2.15. KC is calculated using Equation 2.7. Other parameters are measured values.

In **Table 4.5**, U_{cw} values range from 0.53 to 0.63 which means that the combined flow is current dominated, but the wave effect is also significant. The effect of waves begins to become insignificant when $U_{cw} \geq 0.7$ (Sumer and Fredsøe, 2001), which is supported by the results of experimental research. Although the scour hole shapes were similar to the shapes of those in the current-alone cases, the size of scour hole or downstream deposition characteristics were

significantly different. Another finding with the combined wave and current experiments was that the scour depth almost stopped growing after 1-1.5 hours, but the downstream sediment accumulation continued to move further downstream, which resulted in reducing the maximum accumulation height observed at the beginning of the experiments. Scour depths obtained from the wave and current combined cases are compared with the depths calculated using Equations 2.16 and 2.17 in **Table 4.6**.

Table 4.6. Comparison of Observed Scour Depth with Calculated Values from Other Studies

Test No.	Observed and Calculated Equilibrium Scour Depth (cm)		
	Observed Depth	Sumer and Fredsøe (2002)	Raaijmakers and Rudolph (2008)
7	2.1	1.2	2.1
8	2.3	1.4	2.2
9	2.0	1.4	1.9
10	2.6	1.6	1.5
11	1.6	1.8	2.8
12	1.8	1.9	2.7
13	1.8	1.9	2.5

Table 4.6 shows that the scour depth observed during the two-hour experiments was close to the calculated equilibrium scour depths. The depth values observed in the 50 mm pier experiments agreed more with Raaijmakers and Rudolph's (2008) calculation, whereas the 19 mm pier experiments agreed more with Sumer and Fredsøe's (2002) study.

Inverted truncated cone-shaped scour was observed around the cylinder in all seven of the cases investigated. The shape of the downstream deposit was much smoother than that of the current-alone cases, and with a similar flow velocity, sand was carried much further downstream (**Table 4.5**). This happened because of the wave's capacity to lift the sand up and enable the current to carry it away. As the sand was carried further in these cases, the maximum height of the sediment

accumulation was much lower than in the current-only cases (**Table 4.5**). Overall, the deposits in the wave and current combined cases maintained a somewhat trapezoidal shape (**Figure 4.6**, **Figure 4.7** **Figure 4.8**). Very minimal scour was observed on the downstream end of the pier.

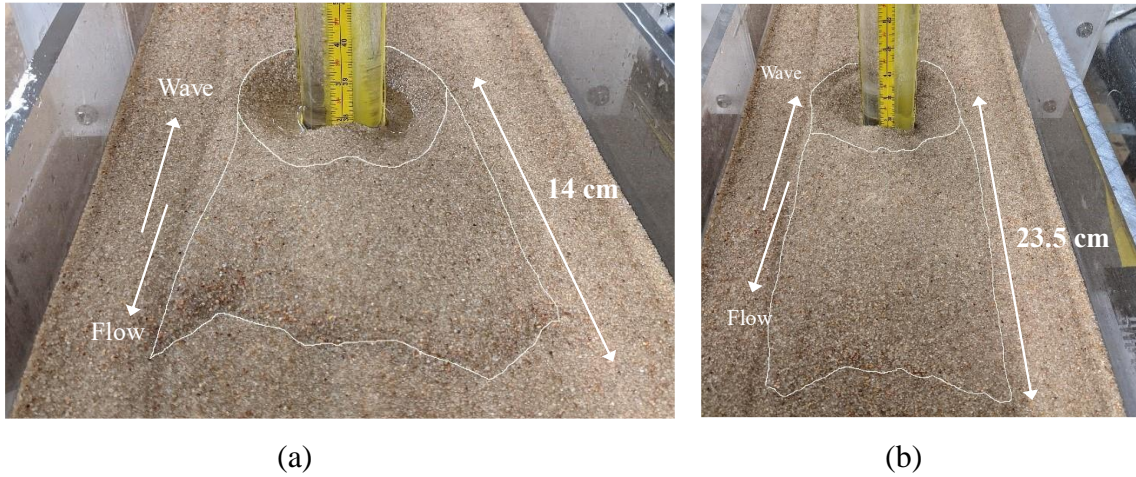


Figure 4.6. Scour around piers in waves and current combined experiments: (a) 50 mm pier, water depth = 15.2 cm, flow velocity = 15.3 cm/s; (b) 50 mm pier, water depth = 17.8 cm, flow velocity = 16.1 cm/s

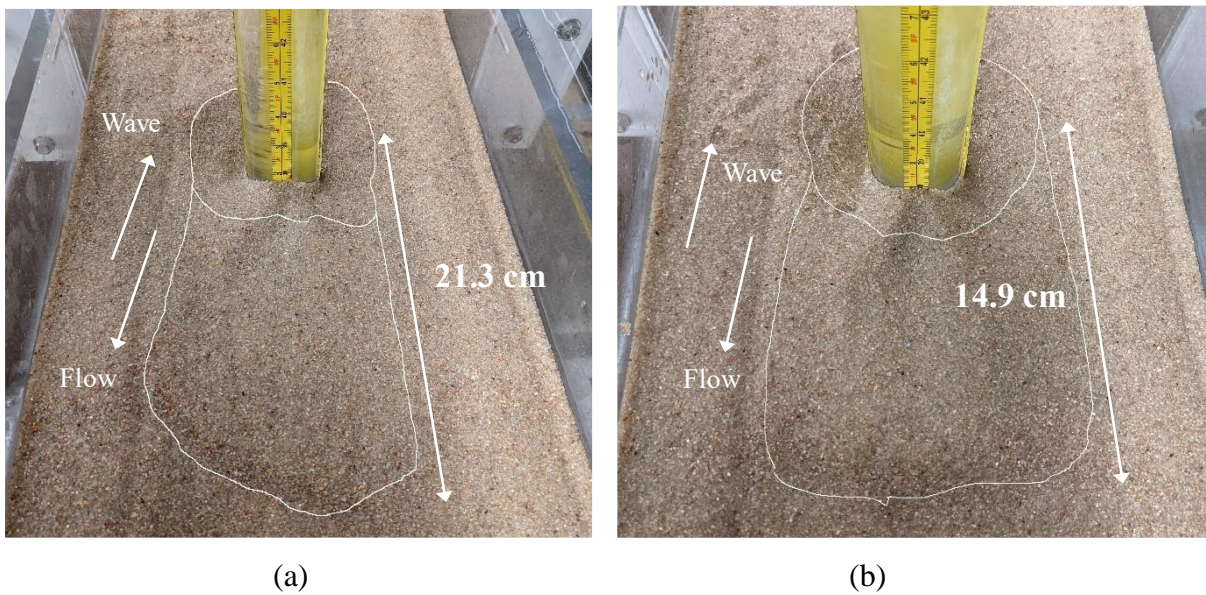


Figure 4.7. Scour around piers in waves and current combined experiments: (a) 50 mm pier, water depth = 20.3 cm, flow velocity = 15.8 cm/s; (b) 50 mm pier, water depth = 25.6 cm, flow velocity = 16.1 cm/s

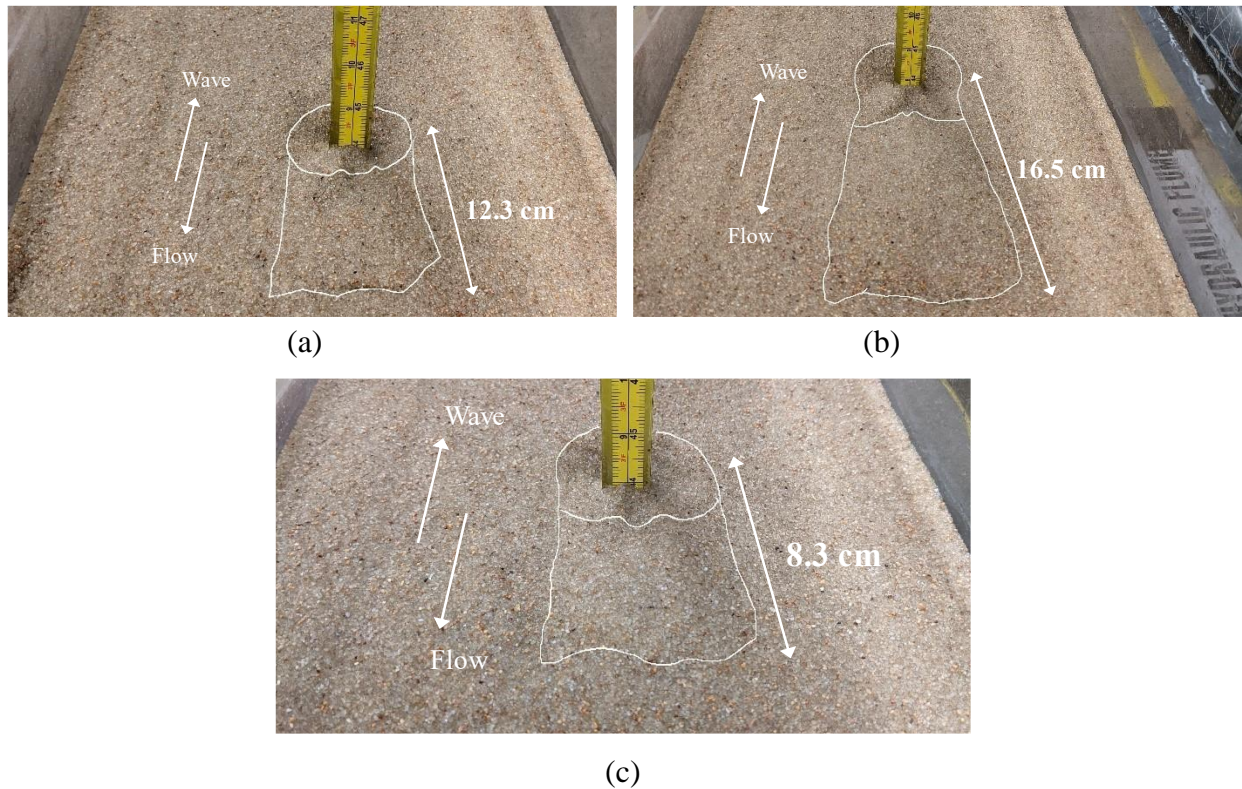


Figure 4.8. Scour around piers in waves and current combined experiments: (a) 19 mm pier, water depth = 15.2 cm, flow velocity = 15.3 cm/s; (b) 19 mm pier, water depth = 17.8 cm, flow velocity = 16.1 cm/s; (c) 19 mm pier, water depth = 20.3 cm, flow velocity = 15.9 cm/s

4.3. Flow Structure Around Piers Subject to Different Flow Conditions

One of the objectives of this study, the investigation of the flow structure around cylindrical piers, was achieved by employing PIV to explore the velocity field around the pier. The PIV traces the seeding particles in the flow and from that generates streamlines. For wave-alone and wave and current combined cases, the challenge was the back-and-forth movement of the flow direction that occurred in every half-period of the wave. For this reason, an average of the data derived from frames containing information on one-half period of the wave, either the wave crest area or the wave trough area, was used (**Figure 4.9**). As waves induce a local flow in the vicinity of the pier, the direction of the flow is the same as the direction of wave propagation in the wave crest area and opposite to the direction of wave propagation in the wave trough area. In the experiments

conducted on current-only cases, wake vortices formed downstream of the pier, but during the experiments on the combined wave and current scenarios, a complex flow environment was created. These features are explored in this section.

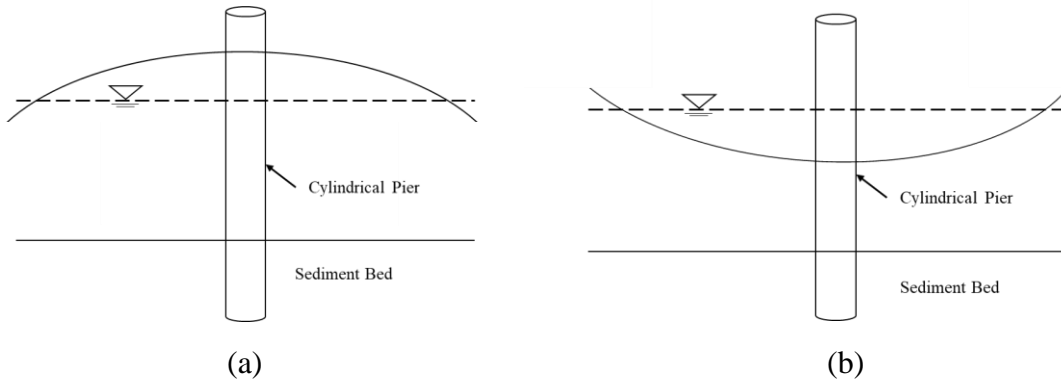


Figure 4.9. (a) Wave crest area crossing the pier, (b) wave trough area crossing the pier

4.3.1. Waves-alone Cases

Six waves-alone scenarios were investigated: three with the 50 mm pier and three with the 19 mm pier. The KC values of the 50 mm pier ranged from 1.96 to 2.31 which corresponds with types C and D of Sumer and Fredsøe's (2006) classification presented in **Figure 2.10**. But the observed flow pattern with the PIV (**Figure 4.10**) corresponded better with types A and B with a suggested KC range of 1.1 to 1.6.

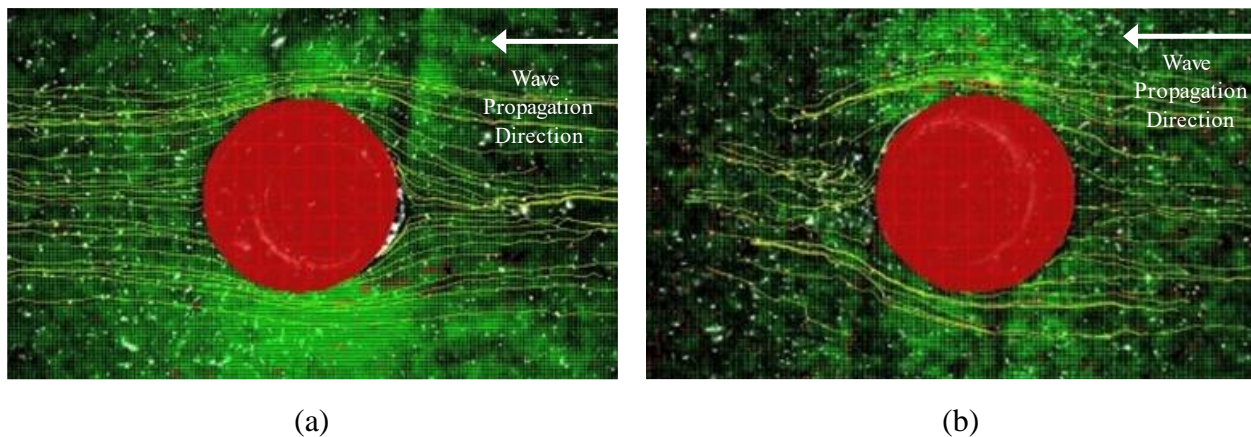


Figure 4.10. Observed flow regimes for KC between 1.96 and 2.31: (a) wave crest area crossing the pier, (b) wave trough area crossing the pier

The range of KC for these types of flow patterns is not widely different, thus a small error in measurement of the flow parameters may lead to mischaracterization of the flow type when compared with Sumer and Fredsøe's (2006) classification. For example, the KC value changes significantly even with a small change in the wave period, wavelength, or wave height. All the parameters were derived from measuring the waves manually in the lab.

According to Sumer and Fredsøe (2006), pairs of asymmetric vortices should be observed in this region (Type E); however, the flow regime for wave-alone cases with KC values ranging from 5.56 to 6.39 depicted in **Figure 4.11** shows partially formed vortices in the wave crest and wave trough areas. The flow patterns resemble Type E downstream of the pier when the wave crest area crosses the pier (**Figure 4.11a**) and upstream of the pier when the wave trough area crosses the pier (**Figure 4.11b**). It needs to be noted that to observe a fully formed vortex in PIV, approximately 5 seconds of flow data is needed to calculate the mean value. But for these wave-alone scenarios, the wave period varied between 0.7s to 0.72 s, with half of the wave period being from 0.35 s to 0.36s. It was not possible to get a pair of fully formed vortices within that time frame using PIV.

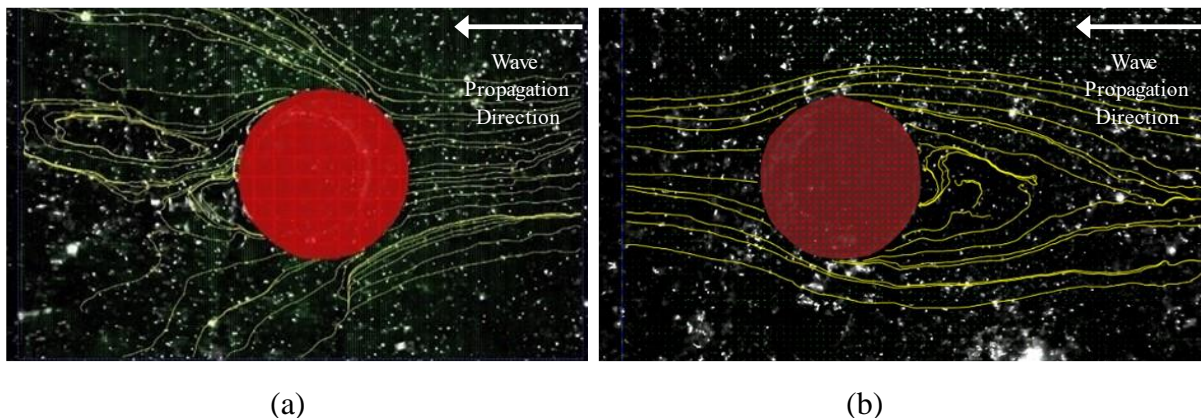
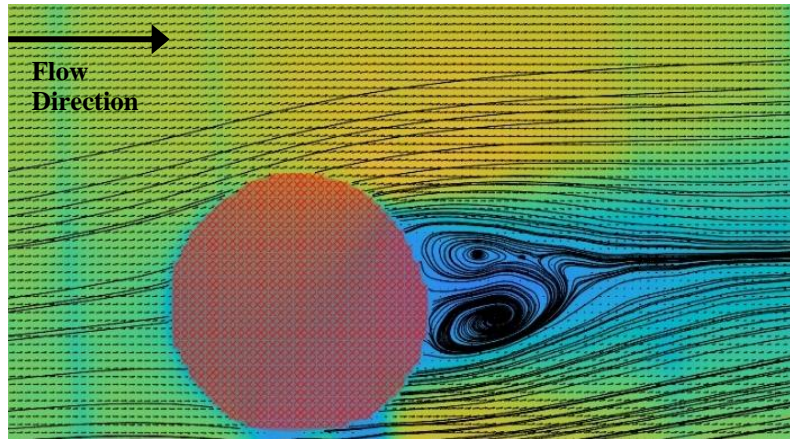


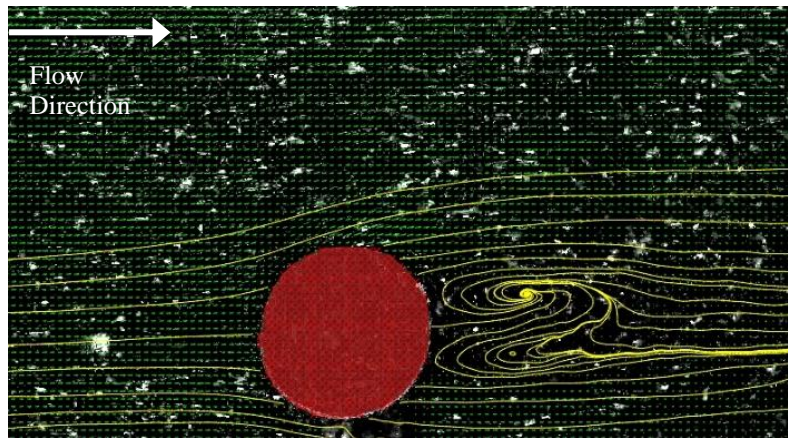
Figure 4.11. Observed flow regimes around pier under wave-only condition with KC range of 5.56-6.39: (a) wave crest area crossing the pier, (b) wave trough area crossing the pier

4.3.2. Current-alone Cases

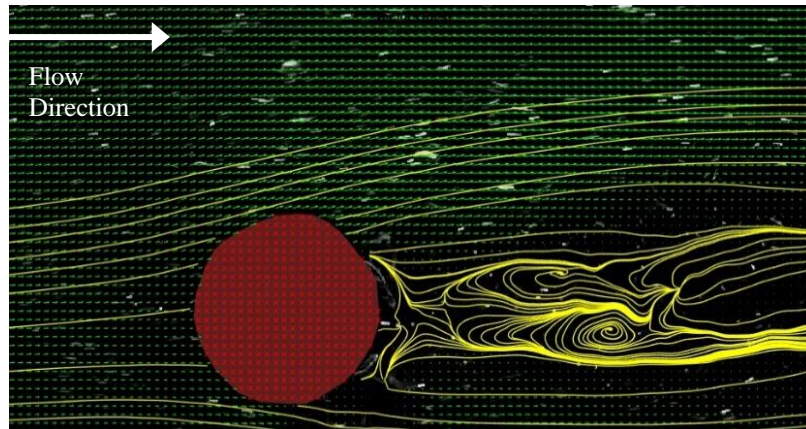
Six scenarios of current-alone cases were investigated in this study, and fully formed vortices were observed in all of them. Their locations, size, and strength varied depending on the flow velocity. The three 19 mm pier cases had an average flow velocity of 15.7 cm/s, 17.4 cm/s, and 27.2 cm/s. Wake vortices were observed immediately downstream of the pier for the cases with 15.7 cm/s and 17.4 cm/s velocities and a distance from downstream of the pier for those with 27.2 cm/s velocity. **Figure 4.12** shows the vortex locations. Test 6 of the current-alone case (water depth = 15.2 cm and flow velocity = 27.2 cm/s) is provided in **Figure 4.13** as an example of the time-averaged velocity distribution around the pier. It can be observed that the flow velocity was very close to 0 immediately upstream of the pier and negative downstream of the pier. The stagnation point where the flow meets the structure justifies the velocity close to zero, and the swirling motion of the vortices resulted in negative velocity downstream of the pier. Although the pier is transparent, it cast a light shadow on the flow and prevented PIV from accurately determining the flow velocity of the region opposite the laser. Since the flow patterns were identical on both sides of the pier, the flow characteristics were only investigated for one side.



(a)



(b)



(c)

Figure 4.12. Observed flow regimes around the 19 mm pier for current alone cases: (a) flow depth = 10.2 cm, flow velocity = 15.7 cm/s; (b) flow depth = 12.70 cm, flow velocity = 17.4 cm/s; and (c) flow depth = 15.2 cm, flow velocity = 27.2 cm/s

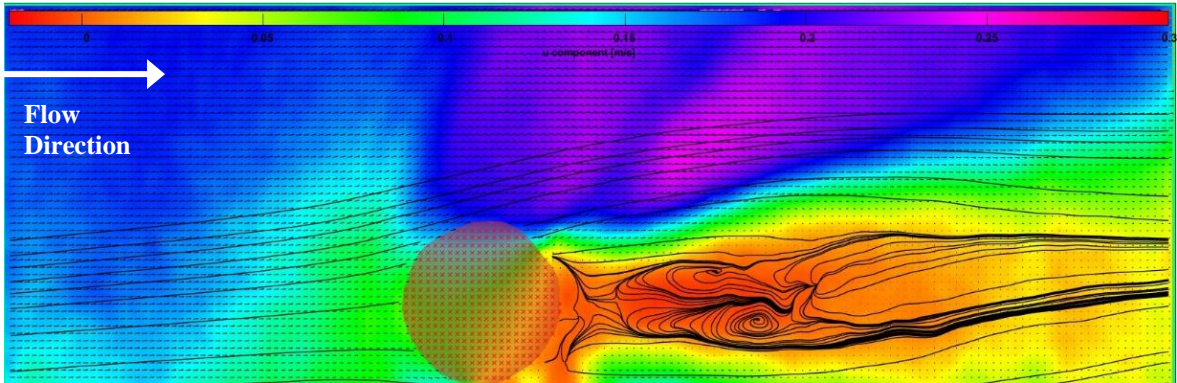
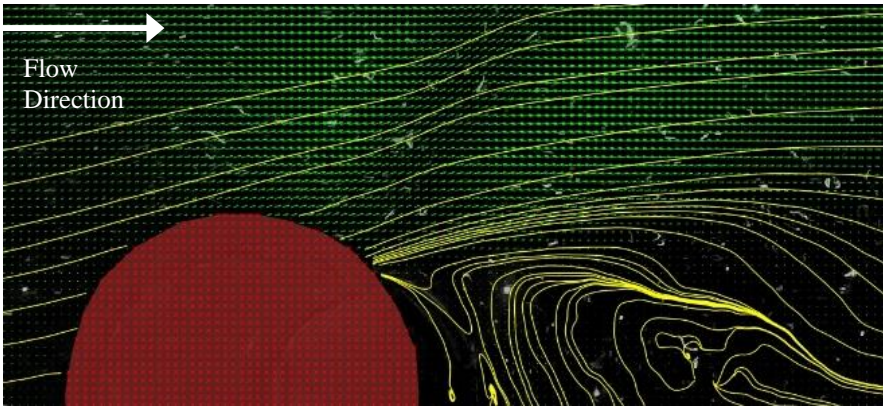
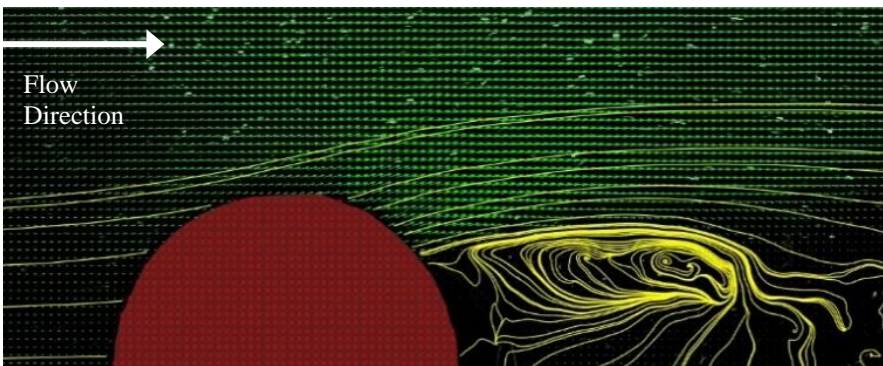


Figure 4.13. Time-averaged velocity distribution around a 19 mm circular cylinder

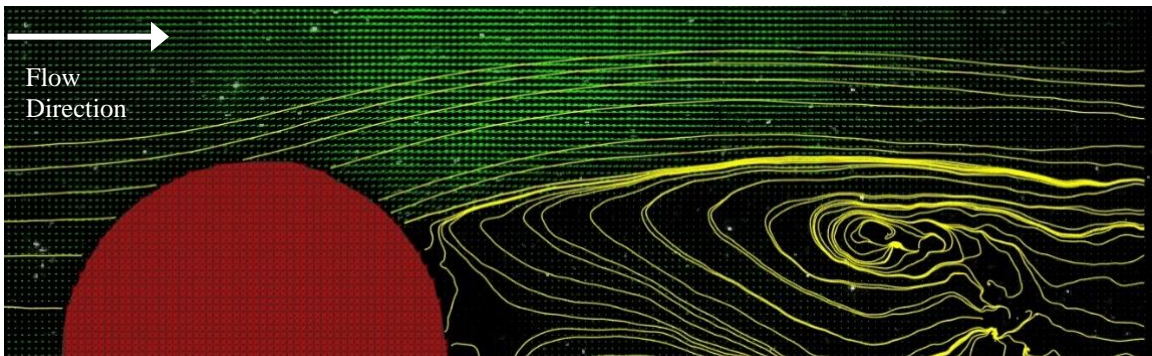
A similar pattern of vortices was observed with the 50 mm pier. The difference in the size of the 19 mm and 50 mm pier vortices meant that just the vortex length and width were different, but all the other characteristics were similar. The size of the vortex around the 50 mm pier increased with the flow velocity and extended further downstream (**Figure 4.14**). **Figure 4.15** represents the time-averaged velocity distribution; the upstream and downstream velocity patterns were similar to those of the 19 mm pier. The length and width of the vortices downstream of the pier provided in **Table 4.7** were measured using PIV. It can be observed that the vortices became larger and stronger with the increased flow velocity. The velocity field and vortex sizes were different for the two piers and the 50-mm pier was associated with much larger and stronger vortices (**Figure 4.14**).



(a)



(b)



(c)

Figure 4.14. Flow regimes around the 50 mm pier for current alone cases: (a) 10.2-cm water depth, 15.9 cm/s velocity; (b) 12.7-cm water depth, 17.4 cm/s velocity; and (c) 15.2-cm water depth, 27.2 cm/s velocity

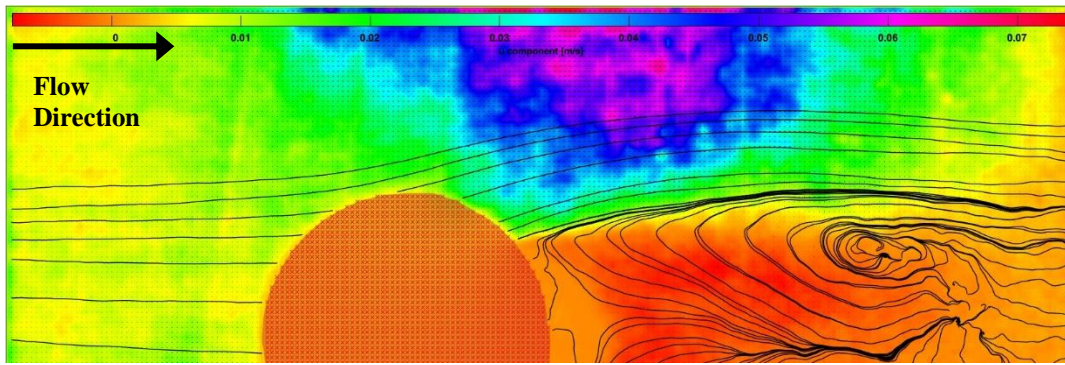


Figure 4.15. Time-averaged velocity distribution around a 50 mm circular cylinder

Table 4.7. Vortex Characteristics Under Different Flow Scenarios of Current-alone Cases

Pier Size	Test No.	Flow Velocity (cm/s)	Length of Vortex (cm)	Width of Vortex (cm)
50 mm	1	15.7	4.1	3.5
	2	17.4	4.7	4.1
	3	27.2	7.1	5.1
19 mm	4	15.9	1.3	1.2
	5	17.4	2.0	1.4
	6	27.2	2.2	1.1

4.3.3. Combined Wave and Current Cases

The flow structure of the seven combined wave and current cases investigated was more complex than the other two previously discussed, due to the interaction between the wave and the current. When the wave crest area crosses the pier, the local flow direction caused by the wave is in the same direction as the wave propagation; however, when the wave trough crosses the pier, the flow direction is opposite to the wave propagation. Both scenarios result in the wave-induced local flow changing its direction. When the current is introduced with waves, in a direction opposite to the wave propagation, the flow features may resemble those shown in **Figure 4.16**.

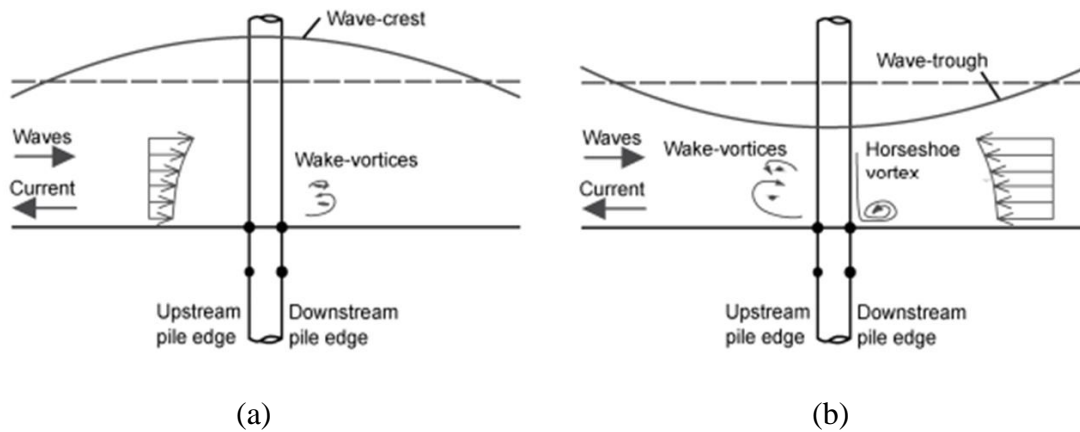


Figure 4.16. (a) Wave-crest area under waves against current, (b) wave trough area under waves against the current (Qi and Gao 2014)

Both horseshoe and wake vortices can be observed in **Figure 4.16**. They were stronger when the wave trough crossed the pier and weaker when the crest crossed the pier, but it was not possible to capture them within a half wave period using PIV as it takes longer than half a wave period to develop a fully formed vortex. Since the PIV can calculate the average displacement of particles within a certain number of frames, the average displacement for the duration of a half-wave was analyzed using PIV, and partially formed vortices were obtained from there (**Figure 4.17a**). The average flow movement was observed in the direction of the current (**Figure 4.17b**).

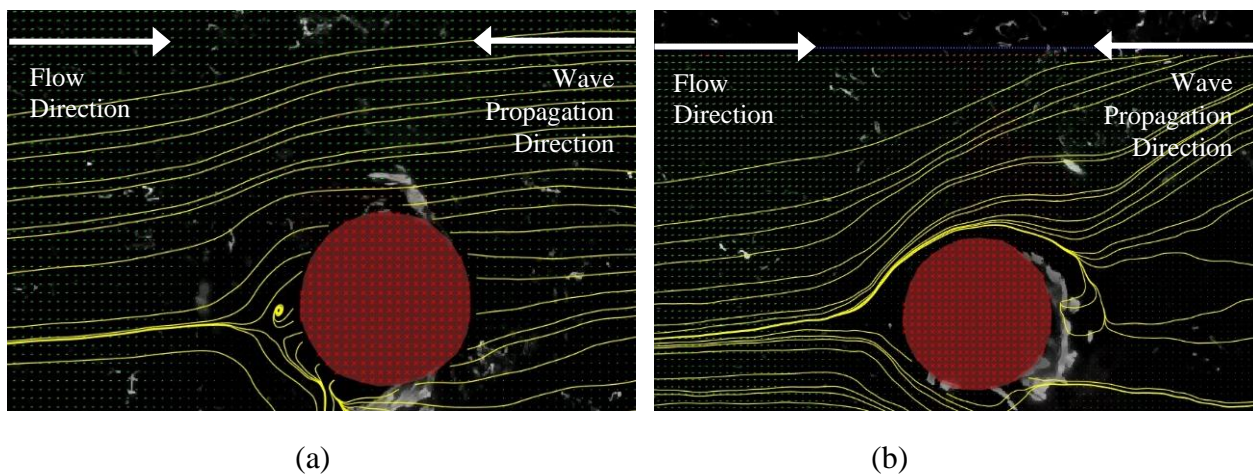
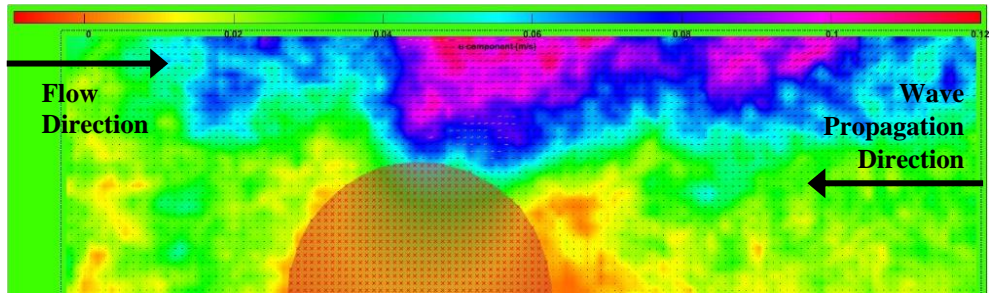


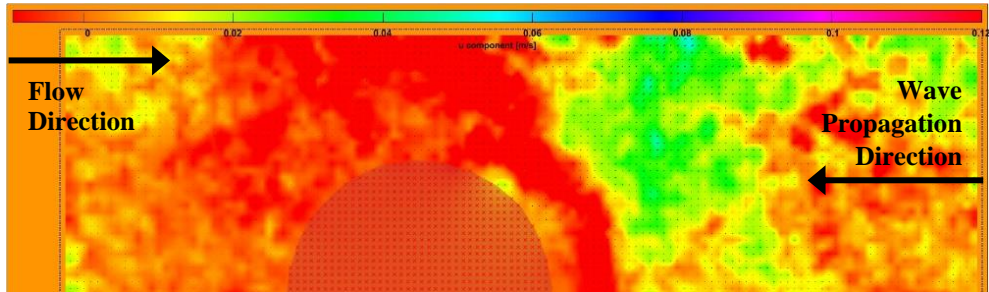
Figure 4.17. Flow pattern for KC range 4.53-5.04 coupled with a current from the opposite direction: (a) wave crest area crossing the pier, (b) wave trough area crossing the pier

The combined velocity of the flow when the wave trough area crossed the pier was larger than when the wave crest crossed the pier. Streamlines produced by PIV verified the fact that the combined wave and current cases are dominated by the current component of the flow.

An interesting flow characteristic was observed from the mean velocity distribution of the wave and current combined cases. When the wave crest crosses the pier, the wave-induced flow direction is opposite to the direction of the current and the combined velocity is smaller than when the wave trough crosses the cylinder (**Figure 4.18**). This implies that the wave-induced local flow nullifies the effect of the current to some extent, but the flow is still current-dominated as the mean flow direction is observed in the direction of the current. This is also why the scour depth observed when waves are against the current is shallower than that of the current-alone conditions. The inverted truncated cone-shaped scour around the pier and the trapezoid-shaped accumulation downstream, observed during the combined wave and current cases are similar to those observed in the current-alone cases.



(a)



(b)

Figure 4.18. Mean velocity field pattern around the 50 mm pier for combined wave and current cases: (a) wave-induced local flow in the same direction as the current direction, and (b) wave-induced local flow in the opposite direction as the current

4.4. Relation Between the Flow Structure Around Piers and the Scour Hole Geometry

Horseshoe and wake vortices are created because of the interaction between flow and structure. Typically, horseshoe vortices are responsible for digging up bed material from the bottom of the channel, and wake vortices are responsible for carrying it away. Since the flow structure around piers dictates the scouring process, it is imperative for predicting scour accurately to understand the flow structure around piers under different flow conditions. In this section, an attempt is made to draw a connection between the geometry of a scour hole and the flow pattern around a pier.

4.4.1. Waves-alone Cases

An irregular pattern, similar to ripples on the surface of the sediment bed near the cylinder, was observed in the geometry of scour holes in waves-alone cases when the KC values were below 6.

A lower KC value means that the orbital velocity is weaker, which makes it more difficult for the waves to pick up the sediment from the bottom of the bed. The PIV showed that the flow separation only occurred downstream. The location of the wave generator is considered the most upstream point for the waves-alone cases. The average displacement information for each half period of the waves was calculated using PIV and showed that in the direction of the wave propagation, the relative velocity was slightly higher than that of the half-wave in the opposite direction. Therefore, the maximum scour depths were observed downstream from the center of the pier (**Figure 4.2**).

The locations of the maximum scour point for the waves-alone cases with KC values > 6 were similar to those with lower values, but the scour pattern was more precise for these cases. A partially developed twin-horn-shaped (THS) scour was observed in these cases. Wave-induced local flow velocity was not strong enough to create horseshoe vortices, which is the reason for no noticeable scour on the upstream and downstream regions. Vortex shedding is the governing factor for scour occurring for KC values between 6 and 100, as at this range, partially formed vortices are created for both wave crest and trough area (**Figure 4.11**). The creation of larger asymmetric vortices in the direction of the wave propagation was observed in this range of KC values, which justifies the creation of a twin-horn shaped scour hole. The scour was more developed lengthwise (9.3 to 16 cm) than sidewise (3.4 to 4.6), which may be attributed to the width of the flume, which could have restricted the natural flow pattern of the sidewise waves.

4.4.2. Current-alone Cases

PIV results for the current-alone cases produced clearly visible fully formed vortices downstream of the pier (**Figure 4.12** and **Figure 4.14**). Their length and width were measured using PIV, and their size and strength increased in correlation with the velocity. As the wake vortices are responsible for carrying the scoured sediment downstream of the pier, the stronger they are, the further they can carry the sediment. The geometry of the scour hole produced during the current-only conditions supports this statement. During the 50 mm pier experiments, it was observed that at the beginning of the scouring process, the horseshoe vortices dominated the scouring process, and sediment was first dug in front of the pier and then gradually expanded sidewise. The scoured bed material was accumulated behind the pier, thus initially, the downstream accumulation was higher and closer to the pier. With strong horseshoe vortices, the scour reached the bottom very quickly, and the experiment was stopped. As a result, the comparatively weaker wake vortices did not have enough time to carry the scoured sediment further downstream. The maximum deposition height was almost 4 cm, which is a significant height for only 3 minutes of scouring. The vortex length and width were measured to gain an indication of their strength, and **Table 4.6** depicts how strong they were. The strong wake vortices carried the sediment downstream and when it decayed into small eddies, deposited it on both sides of the accumulated sediment, creating small horn like extensions on the sides of the primary deposit.

This was even more clear with the 19 mm pier scour pattern. The scour did not reach the bottom of the pier, but the sediment deposited behind the pier continued to move downstream during the two-hour experiment. When the velocity was higher, as shown during Test 6, the downstream deposition almost reached the downstream edge of the sediment bed. The strong wake vortices

carried the sediment downstream. The accumulation height reduced, while the scour depth, length, and width continued to grow.

4.4.3. Combined Waves and Current Cases

Scour is more complex in the combined waves and current cases than in either the wave-only or current-only cases. A steady current always moves in a certain direction, whereas waves change direction every half cycle. In a half cycle of the wave, the direction of wave motion is the same as the current direction, and for the other half cycle, the direction is the opposite. This is important because when the wave propagation direction is opposite to the current direction, the wave-trough area is in the same direction as the current, and the wave crest area is in the opposite direction of the current (Qi and Gao 2014). When wave and flow are in the same direction, strong horseshoe and wake vortices are created, but when they are in the opposite direction, the strength of the wake vortices is greatly reduced, and the horseshoe vortices disappear. The opposite half cycle disrupts the creation of the boundary layer as well and affects the creation of every half cycle horseshoe vortex (HSV). Shorter wave periods result in less scour, as they disrupt the process frequently. Especially, it is observed from PIV that in the direction of wave propagation, wave-induced local velocity is higher than its opposite cycle which is working against the HSV to nullify its effect (**Figure 4.18**). That is why during combined wave and current cases, when the wave propagation is opposite the current direction, the scour depth is shallower than that of the current-induced scour. However, these combined cases are mostly current-dominated, and as a result, the scour shape resembles the current-alone scour shapes but is smaller in size. Wake vortices play an important role in shaping the scour hole. Partially formed wake vortices help to form an inverted truncated cone shape around the cylinder and carry the sediment downstream to create a somewhat trapezoidal-shaped deposit. Since the unidirectional movement of current is disrupted every half

cycle, it was not possible for PIV to trace the average movement of the particles and show a fully formed vortex from frames obtained for only half-wave cycles.

When the water depth is low and the wave is closer to the bottom of the flume, it stirs up the bed material easily and the current component of the combined flow takes it downstream. But when the water is deep, wave-induced local velocity cannot stir up the bed material as easily, so the downstream movement of sediment is reduced. Since the combined wave and current cases are dominated by the current, PIV streamlines show an average movement of water in the current direction; however, it was also observed from the PIV that the opposite movement of the wave disrupts the flow formation of current-induced vortices. **Figure 4.18b** shows the presence of negative velocity in the combined wave and current environment, caused by the wave half cycle moving in the opposite direction of the current.

CHAPTER 5

CONCLUSIONS AND FUTURE RESEARCH RECOMMENDATIONS

5.1. Summary and Conclusions

Scour is one of the most common reasons for the failure of hydraulic structures, and the development of effective measures for mitigating or eliminating these failures requires a comprehensive understanding of the flow behavior around the structure and estimating the scour pattern. Hydraulic structures are commonly seen in three types of flow environments: riverine, coastal, and lacustrine. The current-alone experiments were conducted in a simulated riverine environment in the lab, the waves-alone experiments were conducted in a simulated coastal environment, and the combined wave and current cases were conducted in a simulated lacustrine environment. A cylindrical pier was installed in a sediment bed and tested under different flow conditions to investigate the scour hole geometry around the pier, and PIV was employed to visualize the mean flow field around the pier. A connection between the flow structure around piers and the scour hole geometry was investigated, and the results are summarized below.

Waves-alone Cases

- No definite pattern of scour was observed for KC values lower than 2.5 (for the 50 mm pier), but some irregular scouring and deposition of sediment were seen near the pier. The KC values were slightly higher ($5.5 < KC < 6.5$) for the 19 mm pier, and a partially developed twin-horn-shaped scour pattern was observed.
- Maximum scour depths were located on the sides of the cylindrical pier.
- The PIV results for the waves-alone cases with lower KC values showed flow separation with scattered under-developed vortices. Clearer vortices were observed for the higher KC values

on the downstream side of the pier from the direction of wave propagation, which justified the location of the maximum scoured points around the pier for these cases.

- Since wave-induced local flow velocity was not strong enough to create horseshoe vortices, upstream and downstream scour was not observed.
- Length of scour was much larger than the width of the scour in this study.

Current-alone Cases

- An inverted truncated cone shaped scour hole and a roughly trapezoidal shaped deposition downstream were observed around the pier.
- Since current-alone scours are dominated by the horseshoe vortices, maximum scour depth was observed at the front end of the pier.
- The size and depth of the scour hole and the downstream deposition were directly correlated with the velocity of the flow.
- The PIV results revealed fully formed wake vortices whose size and strength varied with the velocity of the flow. When the velocity was high enough, strong wake vortices carried the sediment away from the pier and created a small horn-shaped extension at the downstream end of the deposited sediment.

Waves and Current combined Cases

- In the combined wave and current environment, the shape of the scour hole and downstream deposition was similar to the shapes observed for the current-alone cases. An inverted truncated cone was observed around the pier and a smooth trapezoid shaped deposition was observed downstream, showing that the combined cases were dominated by the current component of the flow.

- The maximum scour was observed in front of the pier, although in some cases, the scour depth was the same in front of and at the sides of the pier. The scour was not as deep in these cases as in the current-induced scour, and deeper than that induced by waves-only.
- The edges of the tail of the deposition area were smooth and rounded, unlike those of the current-alone cases that had sharper, more defined edges.
- The U_{cw} values varied between 0.53 and 0.63, which proved that the waves were significant in the sediment transport process. The downstream deposition was transported further than in the current-alone cases, especially when the water depth was smaller and waves were generated closer to the ground and stirred up the bed material because the waves could lift the sand and the current could carry it away.

5.2. Recommendations for Future Research

Based on the finding in this study, the challenges faced while conducting the study, and a comprehensive literature review, the following are recommendations for future work.

- The laboratory flume used in this study was not built to sustain the weight of a large volume of sediment; therefore, the depth of the sediment bed was kept small, and under these flow conditions, this depth was not enough for the 50 mm pier to reach equilibrium scour. The flow rate was also restricted to a maximum of 200 gpm, which was the combined capacity of two built-in pumps that were attached to the flume. If future research were conducted in a flume better suited for these kinds of experiments, the researcher could conduct an investigation with a wider range of flow rates and flow velocities. A flume that could handle sediment transport would provide the researcher with the flexibility of working with both clear-water and live-bed flow regimes.

- This study examined only one shape of the pier. Flow structure around piers of other shapes should be investigated to explore the effects of the shape of the pier on the shape, size, and surrounding flow characteristics of local scour.
- The flow structure around a group of piles with different arrangements merits investigation.
- The PIV tool was not suitable for investigating waves, and further research could develop a method to enhance its efficiency. In addition, the effects of pier submergence on local scour could not be determined, as it would have affected the quality of the images obtained from the camera mounted on top. Future research on the effect of pier submergence on local scour under different flow conditions would be helpful.
- Due to the limitation of the experimental facility, a KC number beyond 6.39 could not be generated. Additional research is needed to explore the flow structure around piers with waves having larger KC values.
- The wave generator setup in this study was not ideal. It was modified so that it does not block the recirculation of the flow, but it was still impossible to generate a broader range of flow velocity and wave heights in the flume. Future research could cover the effects of a wider range of these parameters.
- This study only examined waves that propagated against the direction of the current. Future studies could be expanded to study different angles of wave propagation with respect to the direction of the current.
- Only regular waves could be generated in this laboratory flume, and future research that investigates the pattern of irregular waves around piers and the resulting scour would be of value.

References

- Ahamed, T., Duan, J. & Jo, H., 2020. Flood-fragility analysis of instream bridges – consideration of flow hydraulics, geotechnical uncertainties, and variable scour depth. *Structure and Infrastructure Engineering*, pp. 1-14.
- Akhlaghi, E., Babarsad, M. S., Derikvand, E. & Abedini, M., 2020. Assessment of the effects of different parameters to rate scour around single piers and pile groups: a review. *Archives of Computational Methods in Engineering*, 27(1), pp. 183-197.
- Armbrust, S. F., 1982. *Scour about a cylindrical pile due to steady and oscillatory motion*. College Station: Master's Thesis. Texas A&M University.
- Arneson, L., Zevenbergen, L., P.F., L. & Clopper, P., 2012. *Evaluating Scour at Bridges (Fifth Edition)*, s.l.: Federal Highway Administration, U.S. Dept. of Transportation.
- ASTM, 2006. *Standard Practice for Classification of Soils for Engineering Purposes (Unified Soil Classification System)*, s.l.: ASTM International.
- Bozkus, Z. & Yildiz, O., 2004. Effects of inclination of bridge piers on scouring depth. *Journal of Hydraulic Engineering*, Volume 130, p. 827–832.
- Brossard, J. et al., 2009. Principles and applications of particle image velocimetry. *AerospaceLab*, pp. 1-11.
- Chen, B. & Li, S., 2018. Experimental study of local scour around a vertical cylinder under wave-only and combined wave-current conditions in a large-scale flume. *Journal of Hydraulic Engineering*, 144(9).
- Das, S., Ghosh, R., Das, R. & Mazumdar, A., 2014. Clear water scour geometry around circular Piers. *Ecology, Environment and Conservation*, 20(2), pp. 479-492.
- Douglass, S. L. & Webb, B. M., 2020. *Highways in the Coastal Environment: Hydraulic Engineering Circular Number 25 (No. FHWA-HIF-19-059)*, s.l.: Federal Highway Administration. Office of Bridges and Structures.
- Eadie, R. W. & Herbich, J. B., 1986. *Scour About a Single, Cylindrical Pile Due to Combined Random Waves and a Current*. Taipei, American Society of Civil Engineers.
- Ettema, R., Fujita, I., Muste, M. & Kruger, A., 1997. Particle-image velocimetry for whole-field measurement of ice velocities. *Cold Region Science & Technology*, 26(2), pp. 97-112.
- Gautam, P., Eldho, T. I., Mazumder, B. & Behera, M. R., 2019. Experimental study of flow and turbulence characteristics around simple and complex piers using PIV. *Experimental Thermal and Fluid Science*, pp. 193-206.

- Gazi, A. H., Afzal, M. S. & Dey, S., 2019. Scour around piers under waves: Current status of research and its future prospect. *Water*.
- Guo, J., Suaznabar, O., Shan, H. & Shen, J., 2012. *Pier Scour in Clear-Water Conditions with Non-Uniform Bed Materials*, s.l.: Federal Highway Administration (FHWA).
- Hassan, N. H. et al., 2020. *A Review on Applications of Particle Image Velocimetry*. Bangkok, IOP Publishing.
- Horst, M. W., 2009. *Application of Particle Image Velocimetry in Hydraulic Engineering Research*. Vancouver, s.n.
- Huang, R. F., Hsu, C. M. & Lin, W. C., 2014. Flow characteristics around juncture of a circular cylinder mounted normal to a flat plate. *Experimental Thermal and Fluid Science*, Volume 55, pp. 187-199.
- Hunt, B., 2009. *Monitoring scour critical bridges*. s.l.:Transportation Research Board.
- Jensen, M. S. et al., 2006. *Offshore Wind Turbines Situated in Areas with Strong Currents*, Esbjerg: Aalborg University: Offshore Center Denmark .
- Karimi, N., Heidarnejad, M. & Masjedi, A., 2017. A. Scour depth at inclined bridge piers along a straight path: A laboratory study. *Engineering Science and Technology, an International Journal*, 20(4), p. 1302–1307.
- Kawata, Y. & Tsuchiya, Y., 1988. *Local Scour around Cylindrical Piles Due to Waves and Currents Combined*. Costa del Sol-Malaga, American Society of Civil Engineers (ASCE).
- Khan, M. K., Muzzammil, M. & Alam, J., 2016. *Bridge Pier Scour: A review of mechanism, causes and geotechnical aspects*. Aligarh, Aligarh Muslim University.
- Kobayashi, T. & Oda, K., 1994. *Experimental Study on Developing Process of Local Scour around a Vertical Cylinder*. Kobe, Japan, 24th International Conference on Coastal Engineering.
- Kumar, V., Rangaraju, K. & Vittal, N., 1999. Reduction of local scour around bridge piers using slot and collar. *Journal of Hydraulic Engineering*, Volume 125, p. 1302–1305.
- Lacey, G., 1929. *Stable channels in alluviums*. J. Institution of Engineers, Volume 229.
- Lee, G. C., Mohan, S., Huang, C. & Fard, B. N., 2013. *A study of US bridge failures (1980-2012)*, Buffalo, NY: MCEER.
- Liang, B., Du, S., Pan, X. & Zhang, L., 2019. Local Scour for Vertical Piles in Steady Currents: Review of Mechanisms, Influencing Factors and Empirical Equations. *Journal of Marine Science and Engineering*, 8(4).
- Li, J., Yang, Y. & Yang, Z., 2020. Influence of Scour Development on Turbulent Flow Field in Front of a Bridge Pier. *Water*, 12(9).

- Lin, C., Chiu, P. & Shieh, S., 2003. Characteristics of horseshoe vortex system near a vertical plate-base plate juncture. *Experimental Thermal and Fluid Science*, Volume 27, p. 25–46.
- Lloyd, P. M., Stansby, P. K. & Ball, D. J., 1995. Unsteady surface-velocity field measurement using particle tracking velocimetry. *Journal of Hydraulic Research*, 33(4), pp. 519-533.
- Melville, B. W. & Coleman, S. E., 2000. *Bridge Scour*. Littleton, CO: Water Resources Publications, LLC.
- Mia, F. & Nago, H., 2003. Design method of time-dependent local scour at circular bridge pier. *Journal of Hydraulic Engineering*, Volume 129, p. 420–427.
- Miedema, S. A., 2010. *Constructing the Shields curve, a new theoretical approach and its applications*. Beijing, China, s.n.
- Mostafa, Y. E. & Agamy, A. F., 2011. Scour Around Single Pile and Pile Groups Subjected to Waves and Currents. *International Journal of Engineering Science and Technology (IJEST)*.
- National Research Council, 2005. *Assessing and managing the ecological impacts of paved roads*, Washington, D.C.: NRC Press.
- Niedoroda, A. W. & Dalton, C., 1982. A review of the fluid mechanics of ocean scour. *Ocean Engineering*, 9(2), pp. 159-170.
- Niedoroda, A. & Dalton, C., 1982. A review of the fluid mechanics of ocean scour. *Ocean Engineering*, 9(2), pp. 159-170.
- Ozturk, N. A., Akkoca, A. & Sahin, B., 2010. Flow details of a circular cylinder mounted on a flat plate. *Journal of Hydraulic Research*, 46(3), pp. 344-355.
- Ponce, V. M., 2011. *Bridge Scour*. [Online]
Available at: http://ponce.sdsu.edu/bridge_scour.html
[Accessed 7 June 2022].
- Preperneau, U. et al., 2009. Large-scale model study on scour around slender monopiles induced by irregular waves. *Coastal Engineering*, p. 2707–2716.
- Qi, W.-G. & Gao, F.-P., 2014. Equilibrium scour depth at offshore monopile foundation in combined waves and current. *Science China Technological Sciences*, 57(5), p. 1030–1039.
- Qi, W.-G. & Gao, F.-P., 2014. Physical modeling of local scour development around a large-diameter monopile in combined waves and current. *Coastal Engineering*, pp. 72-81.
- Raaijmakers, T. & Rudolph, D., 2008. *Time-dependent scour development under combined current and waves conditions - laboratory experiments with online monitoring technique*. s.l., s.n.
- Raikar, R. & Dey, S., 2005. Clear-water scour at bridge piers in fine and medium gravel beds. *Canadian Journal of Civil Engineering*, 32(4), pp. 775-781.

- Raudkivi, A. J. & Ettema, R., 1983. Clear-Water Scour at Cylindrical Piers. *Journal of Hydraulic Engineering*, 109(3).
- Richardson, E. & Davis, S., 2001. *Evaluating scour at bridges (Fourth Edition)*, s.l.: Federal Highway Administration, U.S. Dept. of Transportation.
- Schanderl, W., Jenssen, U., Strobl, C. & Manhart, M., 2017. The structure and budget of turbulent kinetic energy in front of a wall-mounted cylinder. *Journal of Fluid Mechanics*, Volume 827, pp. 285-321.
- Sim, L. N. & Fane, A. G., 2017. 4.4 Advanced Monitoring of Membrane Fouling and Control Strategies. In: E. Drioli, L. Giorno & E. Fontananova, eds. *Comprehensive Membrane Science and Engineering*. s.l.:Elsevier, pp. 72-103.
- Sreedhara, B. M., Manu, M. & Pruthviraj, U., 2015. *Comparative Study on different Bridge Scour Monitoring Techniques: A Review*. Roorkee, HYDRO 2015 INTERNATIONAL 20th International Conference on Hydraulics, Water Resources and River Engineering.
- Sumer, B. M. & Fredsøe, J., 2006. *Hydrodynamics Around Cylindrical Structures*. Revised Edition ed. s.l.:World Scientific Publishing Co. Pte. Ltd..
- Sumer, M. B. & Fredsøe, J., 2001. Scour around Pile in Combined Waves and Current. *Journal of Hydraulic Engineering*, 127(5), pp. 403-411.
- Sumer, M. B. & Fredsøe, J., 2002. *The Mechanics of Scour in the Marine Environment*. s.l.:World Scientific.
- Sumer, M., Christiansen, N. & Fredsøe, J., 1992. *Time scale of scour around a vertical pile*. San Francisco, CA, USA, Second International Offshore and Polar Engineering Conference.
- Sumer, M., Christiansen, N. & Fredsøe, J., 1993. Influence of Cross Section on Wave Scour around Piles. *Journal of Waterway, Port, Coastal, and Ocean Engineering*, 119(5), p. 477–495.
- Thielicke, W. & Stamhuis, E., 2014. PIVlab—towards user-friendly, affordable and accurate digital particle image velocimetry in MATLAB. *Journal of Open Research Software*, 2(1).
- Thomas, G., 2021. *Scouring in Bridge & Mitigation | Scour mechanism | Types*. [Online] Available at: <https://engineeringcivil.org/articles/bridge/scouring-in-bridge-mitigation-scour-mechanism-types/> [Accessed 14 June 2022].
- Unger, J. & Hager, W. H., 2007. Down-flow and horseshoe vortex characteristics of sediment embedded bridge piers. *Experiments in Fluids*, pp. 1-19.
- Unsworth, C. A., 2015. Particle Imaging Velocimetry. *British Society for Geomorphology*, pp. 1-15.

- Wang, J., 2004. *The SRICOS-EFA method for complex pier and contraction scour*. College Station, Texas: Doctoral Dissertation, Texas A&M University.
- Webb, B. & Matthews, M., 2014. Wave-induced scour at cylindrical piles: estimating equilibrium scour depth in a transition zone. *Journal of the Transportation Research Board*, 2436(1), p. 148–155.
- Wensworth, C. K., 1922. A Scale of Grade and Class Terms for Clastic Sediments. *The Journal of Geology*.
- Williams, P., Balachandar, R., Roussinova, V. & Barron, R., 2019. *PIV Measurements Around A Submerged Cylinder With Local Scour Protection*. Panama City, 38th IAHR World Congress.
- Williams, P., Balachandar, R., Roussinova, V. & Barron, R., 2021. *Particle Image Velocimetry (PIV) Investigation of Local Scour Around Emergent and Submerged Circular Cylinders*. Galway, 8th International Junior Researcher and Engineer Workshop on Hydraulic Structures (IJREWHS 2021).
- Williams, P., Balachandar, R., Roussinova, V. & Barron, R., 2022. Particle image velocimetry evaluation of flow-altering countermeasures for local scour around a submerged circular cylinder. *International Journal of Sediment Research*, 37(4), pp. 411-423.
- Wilson, K. V., 1995. *Scour at selected bridge sites in Mississippi*, Jackson, Mississippi: U.S. Geological Survey.
- Zanke, U. C. E. et al., 2011. Equilibrium scour depths around piles in noncohesive sediments under currents and waves. *Coastal Engineering*, 58(10).
- Zyserman, J. & Fredsøe, J., 1988. *Numerical Simulation of Concentration Profiles of Suspended Sediment. Under Irregular Waves*, Copenhagen, Denmark: Technical University of Denmark.

APPENDIX A

SAMPLE CALCULATIONS

Calculation of the Keulegan-Carpenter (KC) Number

A sample calculation of the Keulegan-Carpenter (KC) number from **Table 3.1** is provided here.

The calculation of the first row of that table is shown below:

$$\text{Keulegan Carpenter Number, } KC = \frac{U_m T}{D}$$

Here, U_m is the maximum wave-induced velocity, T is the wave period, and D is the pier diameter.

T and D were measured at the laboratory.

Maximum wave-induced velocity,

$$U_m = \frac{\pi H}{T} \times \left(\frac{1}{\cosh[kd]} \right) = \frac{\pi H}{T} \times \left(\frac{1}{\cosh\left[\frac{2\pi}{L} \times d\right]} \right) = \frac{\pi \times 7.62}{0.7} \times \left(\frac{1}{\cosh\left[\frac{2\pi}{70.46} \times 15.24\right]} \right) = 16.48 \text{ cm/s}$$

$$\text{So, } KC = \frac{U_m T}{D} = \frac{16.48 \times 0.7}{5} = 2.31$$

Determination of the Sediment Size (d_{50})

Table A.1 shows the calculation of the sediment size (d_{50}) required to maintain a clear water flow regime at different water depths for the sediment bed installed in the flume. The rows marked with red mean either that the trial sediment diameter was bigger than 2mm or its associated mobility number was bigger than 0.7. 2mm is the threshold at which it is considered granules, not sand, (**Figure A.1**). And beyond the mobility number of 0.7, the flow regime is considered the transition zone. Attempts were made to keep the sediment as small as possible and the mildest slope achievable in the laboratory flume (0.00032). A mobility number ≤ 0.7 , corresponding to a certain

sediment diameter, confirms that the flow shear stress is smaller than the critical shear stress of the sediment with that diameter and the sediment will not move.

Sample calculation for the second row of **Table A.1** is shown below:

$$\text{Hydraulic Radius, } R = \frac{\text{Area}}{\text{Wetted Perimeter}} = \frac{15.24 \times 30}{2 \times 15.24 + 30} = 7.56 \text{ cm}$$

$$\text{Velocity, } u = \frac{\text{Flow Rate}}{\text{Area}} = \frac{0.012}{0.15 \times 0.30} = 0.27 \text{ m/s}$$

$$\text{Roughness Reynolds Number, } V_* = \sqrt{gRS} = \sqrt{9.81 \times 0.0756 \times 0.00032} = 0.15 \text{ m/s}$$

(Here, g is the gravitational acceleration and S is the slope)

$$\text{Mobility Number, } Y = \frac{\tau}{(\rho_s - \rho_w)gd_{50}} = \frac{gRS}{(\rho_s - \rho_w)gd_{50}} = \frac{9.81 \times 0.0756 \times 0.00032}{(2.65 - 1) \times 9.81 \times 0.0006} = 0.024$$

Y_{cr} is mobility number at the critical stage indicating the stage of inception of sediment transport.

This value is obtained from the Shields diagram (**Figure A.2**)

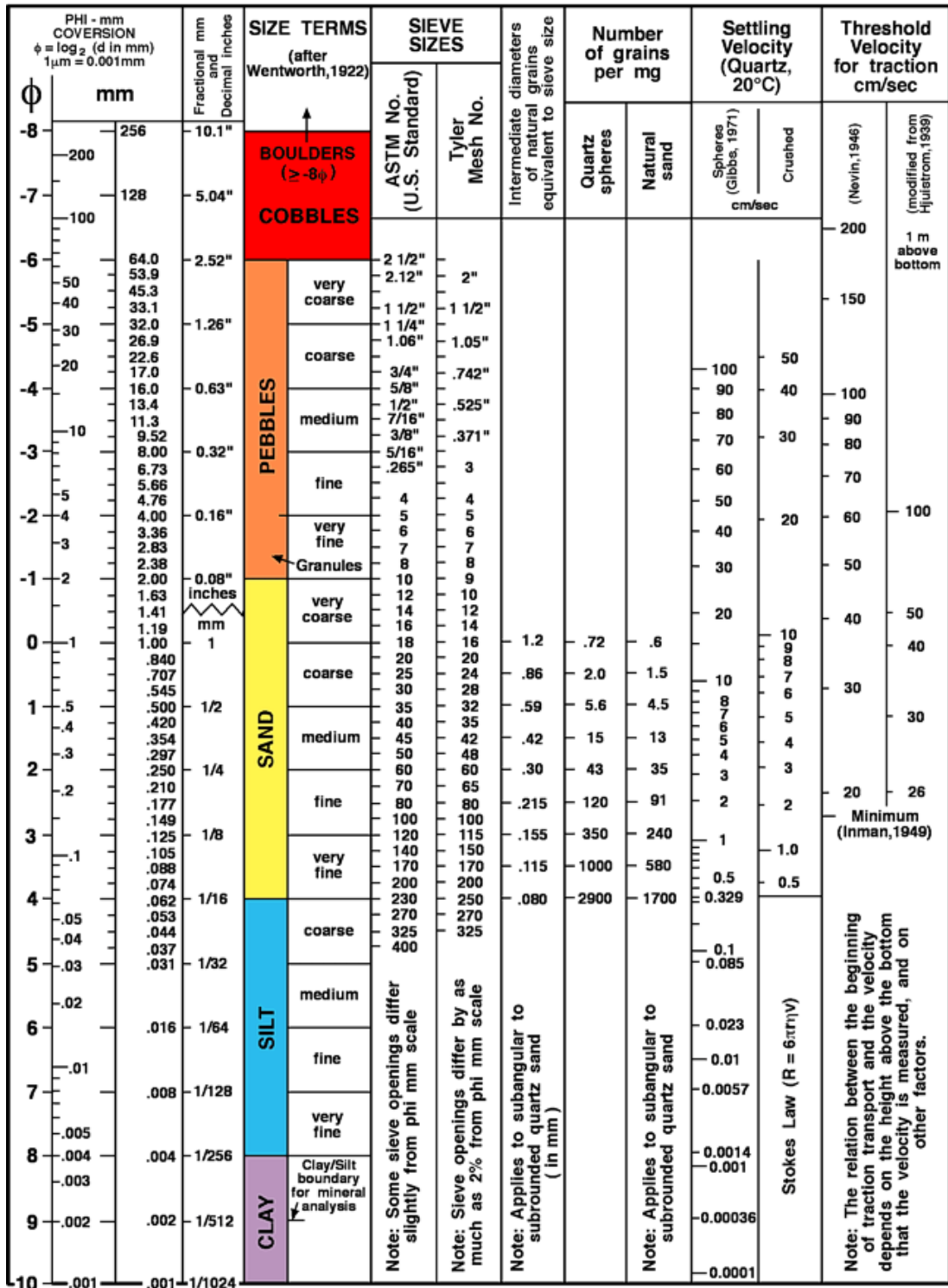


Figure A.1. Grain size classification chart (Wensworth, 1922)

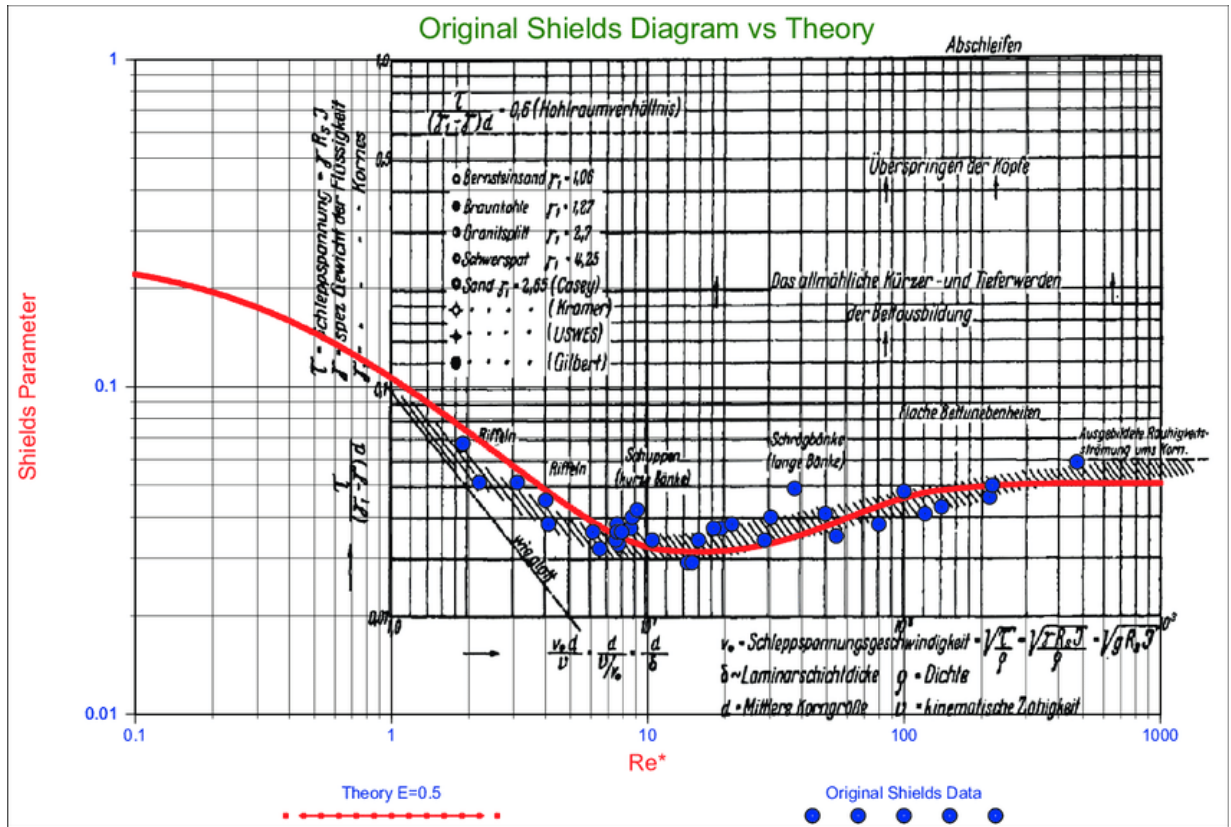


Figure A.2. Shields diagram (adopted from Miedema, 2010)

Table A.1. Determination of Appropriate Sediment Size to Maintain a Clear-Water Regime

	h (cm)	B (cm)	R _h (cm)	S	Q (cfs)	Q (cms)	u (m/s)	V* (m/s)	D (mm)	Re*	Y	Y _{cr}	M
Set 1	15.2	30.0	7.56	0.0003	0.44	0.012	0.272	0.015	0.600	8.949	0.023	0.032	0.8
	15.2	30.0	7.56	0.0003	0.44	0.012	0.272	0.015	0.650	9.695	0.021	0.032	0.7
	15.2	30.0	7.56	0.0003	0.44	0.012	0.272	0.015	1.000	14.916	0.014	0.033	0.5
	15.2	30.0	7.56	0.0003	0.44	0.012	0.272	0.015	1.800	26.848	0.008	0.039	0.2
	15.2	30.0	7.56	0.0003	0.44	0.012	0.272	0.015	2.000	29.831	0.007	0.040	0.2
Set 2	17.8	30.0	8.14	0.0003	0.44	0.012	0.233	0.015	0.600	9.284	0.025	0.033	0.8
	17.8	30.0	8.14	0.0003	0.44	0.012	0.233	0.015	0.700	10.832	0.021	0.033	0.7
	17.8	30.0	8.14	0.0003	0.44	0.012	0.233	0.015	1.100	17.021	0.013	0.033	0.5
	17.8	30.0	8.14	0.0003	0.44	0.012	0.233	0.015	1.800	27.853	0.008	0.033	0.3
	17.8	30.0	8.14	0.0003	0.44	0.012	0.233	0.015	2.000	30.948	0.007	0.032	0.3
Set 3	20.3	30.0	8.63	0.0003	0.44	0.012	0.204	0.016	0.700	11.156	0.022	0.032	0.8
	20.3	30.0	8.63	0.0003	0.44	0.012	0.204	0.016	0.750	11.952	0.021	0.032	0.7
	20.3	30.0	8.63	0.0003	0.44	0.012	0.204	0.016	1.100	17.530	0.014	0.033	0.5
	20.3	30.0	8.63	0.0003	0.44	0.012	0.204	0.016	1.900	30.279	0.008	0.040	0.3
	20.3	30.0	8.63	0.0003	0.44	0.012	0.204	0.016	2.000	31.873	0.008	0.032	0.3
Set 4	22.9	30.0	9.06	0.0003	0.44	0.012	0.182	0.016	0.700	11.428	0.024	0.032	0.8
	22.9	30.0	9.06	0.0003	0.44	0.012	0.182	0.016	0.750	12.245	0.022	0.032	0.7
	22.9	30.0	9.06	0.0003	0.44	0.012	0.182	0.016	0.800	13.061	0.021	0.032	0.7
	22.9	30.0	9.06	0.0003	0.44	0.012	0.182	0.016	1.900	31.020	0.009	0.040	0.3
	22.9	30.0	9.06	0.0003	0.44	0.012	0.182	0.016	2.000	32.653	0.008	0.032	0.3
Set 5	25.5	30.0	9.45	0.0003	0.44	0.012	0.163	0.017	0.750	12.508	0.023	0.032	0.8
	25.5	30.0	9.45	0.0003	0.44	0.012	0.163	0.017	0.800	13.341	0.021	0.032	0.7
	25.5	30.0	9.45	0.0003	0.44	0.012	0.163	0.017	1.200	20.012	0.014	0.033	0.5
	25.5	30.0	9.45	0.0003	0.44	0.012	0.163	0.017	1.800	30.018	0.010	0.042	0.3
	25.5	30.0	9.45	0.0003	0.44	0.012	0.163	0.017	2.000	33.353	0.009	0.032	0.3

APPENDIX B

GRADATION ANALYSIS

Sediment Samples

Sample: 1

Sample Weight: 500 g

Table B.1. Gradation Analysis of Sediment Bed Soil (Sample 1)

Sieve No.	Sieve Size (mm)	Sieve Weight (g)	Sieve + Material Weight (g)	Material Retained (g)	% Retained on Sieve	Cumulative % Retained on Sieve	Percent Finer, %
#16	1.19	641.9	647.7	5.8	1.2	1.2	98.8
#18	1.00	614.1	765.4	151.3	30.3	31.5	68.5
#20	0.84	631.4	938.4	307.0	61.4	92.9	7.1
#25	0.71	611.3	644.1	32.8	6.6	99.4	0.6
#30	0.60	432.1	434.7	2.6	0.5	99.9	0.1
Pan		481.1	481.6	0.5	0.1	100.0	0.0
				500.0			

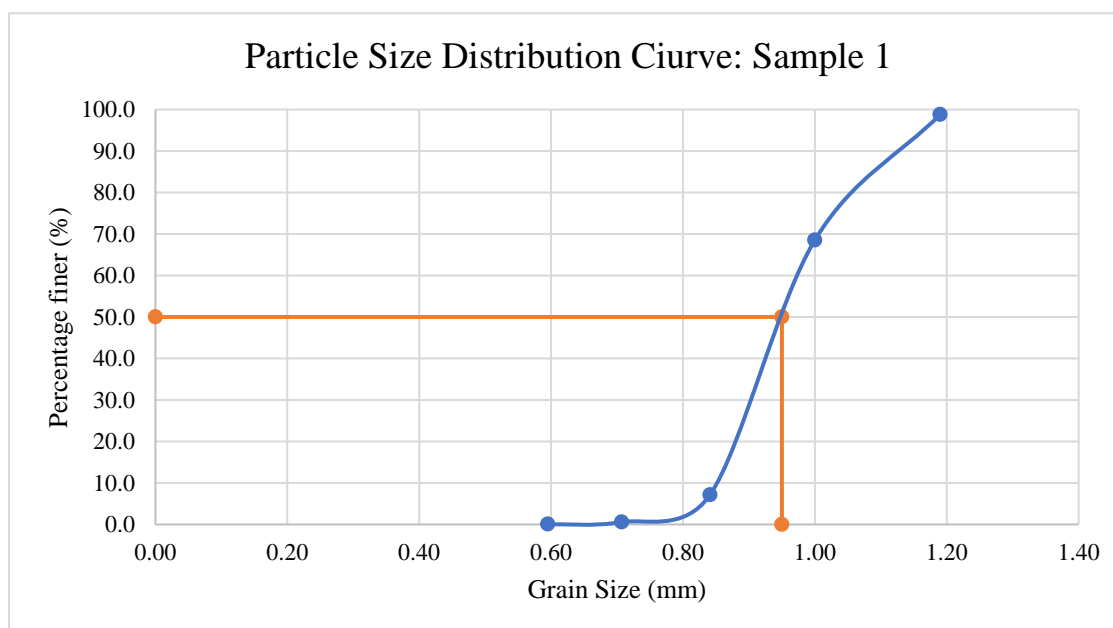


Figure B.1. Sieve analysis of sediment bed soil (Sample 1)

d_{50}	0.95	d_{84}	1.10	d_{16}	0.86	σ_g	1.27
----------	------	----------	------	----------	------	------------	------

Sample: 2

Sample Weight: 500 g

Table B.2. Gradation Analysis of Sediment Bed Soil (Sample 2)

Sieve No.	Sieve Size (mm)	Sieve Weight (g)	Sieve + Material Weight (g)	Material Retained (g)	% Retained on Sieve	Cumulative % Retained on Sieve	Percent Finer, %
#16	1.19	642.0	648.0	6.0	1.2	1.2	98.8
#18	1.00	614.4	780.8	166.4	33.3	34.5	65.5
#20	0.84	631.7	925.3	293.6	58.7	93.2	6.8
#25	0.71	611.3	642.6	31.3	6.3	99.5	0.5
#30	0.60	431.9	434.2	2.3	0.5	99.9	0.1
Pan		481.2	481.6	0.4	0.1	100.0	0.0
				500.0			

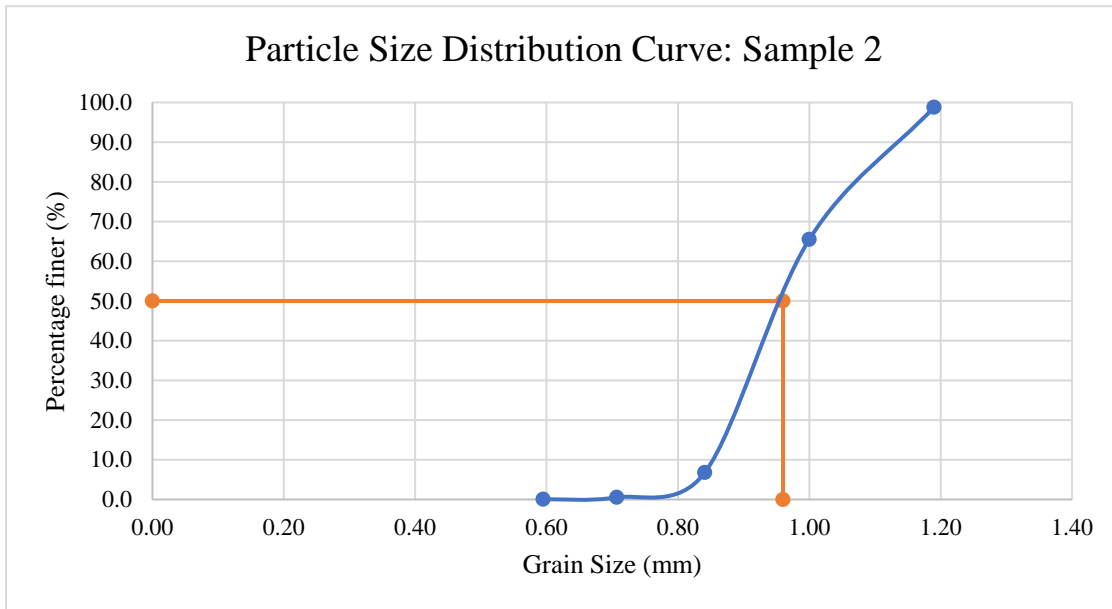


Figure B.2. Sieve Analysis of sediment bed soil (Sample 2)

d_{50}	0.96	d_{84}	1.11	d_{16}	0.87	σ_g	1.28
----------	------	----------	------	----------	------	------------	------

Sample: 3

Sample Weight: 500 g

Table B.3. Gradation Analysis of Sediment Bed Soil (Sample 3)

Sieve No.	Sieve Size (mm)	Sieve Weight (g)	Sieve + Material Weight (g)	Material Retained (g)	% Retained on Sieve	Cumulative % Retained on Sieve	Percent Finer, %
#16	1.19	642.0	648.8	6.8	1.4	1.4	98.6
#18	1.00	614.6	770.5	155.9	31.2	32.6	67.4
#20	0.84	631.8	934.0	302.2	60.4	93.0	7.0
#25	0.71	611.4	643.1	31.7	6.3	99.4	0.6
#30	0.60	431.9	434.6	2.7	0.5	99.9	0.1
Pan		481.1	481.8	0.7	0.1	100.0	0.0
				500.0			

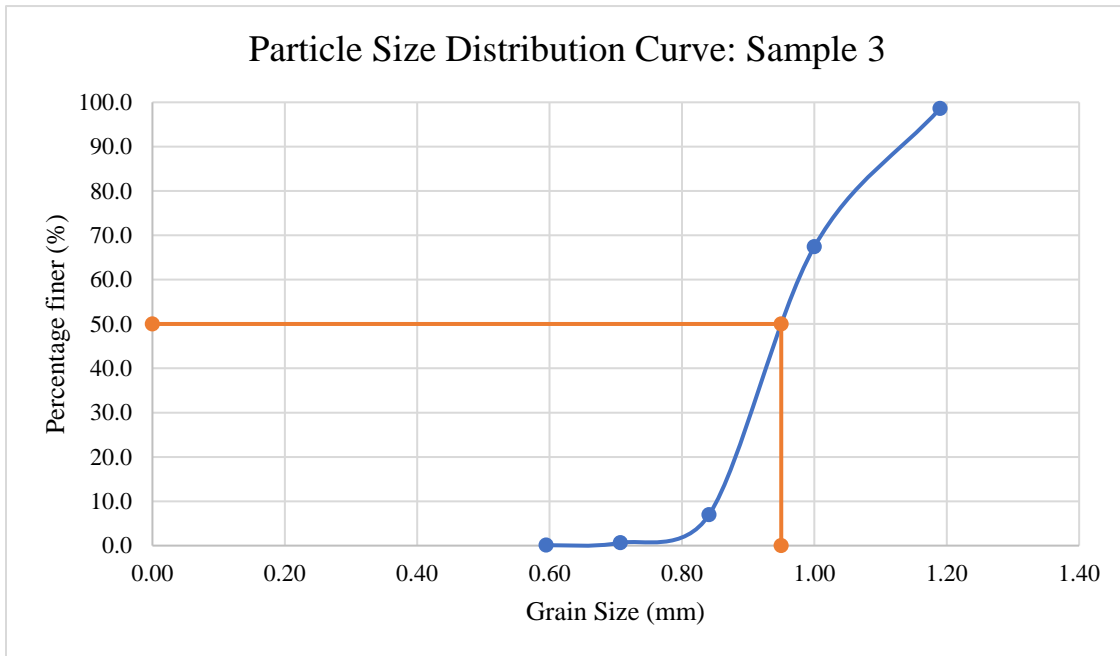


Figure B.3. Sieve Analysis of sediment bed soil (Sample 3)

d_{50}	0.95	d_{84}	1.10	d_{16}	0.86	σ_g	1.27
----------	------	----------	------	----------	------	------------	------